MINERALOGY, PETROLOGY, AND OXYGEN ISOTOPIC COMPOSITIONS OF ALUMINUM-RICH CHONDRULES FROM UNEQUILIBRATED ORDINARY AND THE DAR AL GANI 083 (CO3.1) CHONDRITE

Samuel Ebert[1*], Kazuhide Nagashima[2], Addi Bischoff[1], Jasper Berndt[3] and Alexander N. Krot[2]

[1]Institut für Planetologie, Westfälische Wilhelms-Universität Münster, Germany.

[2]School of Ocean, Earth Science and Technology, Hawai‘i Institute of Geophysics and Planetology, University of Hawai‘i at Mānoa, USA.

[3]Institut für Mineralogie, Westfälische Wilhelms-Universität Münster, Germany

*E-mail address of the corresponding author: samuel.ebert@uni-muenster.de

Abstract. Understanding the genetic relationship between different chondritic components will help to decipher their origin and dynamical evolution within the protoplanetary disk. Here, we obtain insight into these processes by acquiring O-isotope data from 17 Al-rich chondrules from unequilibrated ordinary chondrites (OCs, petrologic type ≤3.2) and four Al-rich chondrules from the CO3.1 carbonaceous chondrite Dar al Gani (DaG) 083. These particular kinds of chondrules are of special interest, as it is suggested that their precursors may have contained refractory material related to Ca,Al-rich inclusions (CAIs) and amoeboid olivine aggregates (AOAs).

The four investigated Al-rich chondrules from the CO3.1 chondrite Dar al Gani 083 consist of olivine, low-Ca pyroxene, Ca pyroxene, and spinel phenocrysts embedded in mostly Na-rich glassy mesostasis. Two chondrules have a homogeneous O-isotopic composition and two are heterogeneous in composition. One chondrule contains relict spinel grains with a $\Delta^{17}O$ value of −24.3±1.3‰, indicative of ^{16}O-rich precursor refractory material, similar to constituents of CAIs and AOAs. The presence of CAI-like precursors for the Al-rich chondrules from CO chondrites is consistent with their previously reported presence of ^{50}Ti excesses (Ebert et al., 2018).

The Al-rich chondrules in the ordinary chondrites studied consist of olivine, low-Ca pyroxene, Ca pyroxene, and, occasionally, spinel phenocrysts embedded in mostly Na-rich glassy mesostasis. Hibonite is present in one Al-rich chondrule. The vast majority of these chondrules have heterogeneous O-isotopic compositions: Chondrule glasses are ^{16}O-depleted compared to chondrule phenocrysts; the $\Delta^{17}O$ values of the former approach those of aqueously

formed fayalite and magnetite grains in type 3 OCs, ~ +5‰. We infer that the chondrule glasses experienced O-isotope exchange with an aqueous fluid on the OC parent asteroids.

Chondrule phenocrysts, like spinel, olivine, low-Ca pyroxene, and Ca pyroxene, were not affected by this isotope exchange and preserved their initial O-isotope compositions. The phenocrysts within individual chondrules have similar $\Delta^{17}O$, whereas the inter-chondrule $\Delta^{17}O$ values range from −4.5 to +1.4‰, i.e., they are in general ^{16}O enriched relative to the majority of ferromagnesian type I and type II porphyritic chondrules in OCs having $\Delta^{17}O$ of ~ +1‰. Because no relict grains were identified in the Al-rich chondrules from ordinary chondrites, the original O-isotopic composition of the refractory precursor material remains unknown.

Additional detailed Na measurements within olivine grains show no major changes in the Na content of the chondrule melt during their crystallization. This implies either that the Na was part of the precursor material or that the Na was enriched in the chondrule melt/glass after crystallization of the olivines.

1. INTRODUCTION

Understanding a potential genetic link between chondrules and refractory inclusions [Ca,Al-rich inclusions (CAIs) and amoeboid olivine aggregates (AOAs)] is an important goal in cosmochemistry. Relict CAIs and AOAs found within chondrules from ordinary (OCs) and carbonaceous chondrites (CCs) indicate that CAIs were present in the chondrule-forming regions, but only some of them experienced melting during chondrule formation (e.g., Krot et al., 2002, 2004, 2006a, 2017a; Nagashima et al., 2020; Zhang et al., 2020). These observations are interpreted as evidence for a localized nature of chondrule-forming events (Krot, 2019).

Aluminum-rich (>10 wt% bulk Al_2O_3) chondrules, occurring in all chondrite groups, are of special interest as they have been suggested to have formed from precursors containing refractory CAI- and/or AOA-like objects (Nagahara and Kushiro, 1982; Bischoff and Keil, 1983a,b, 1984; Bischoff et al., 1985, 1989; Krot and Rubin, 1994; Krot and Keil, 2002; Russell et al., 2000; MacPherson and Huss, 2005; Guan et al., 2006; Rout and Bischoff, 2008; Zhang and Hsu, 2009; Ebert and Bischoff, 2016; Ebert et al., 2018, 2019; Zhang et al., 2020). However, because Al-rich chondrules are relatively common in non-carbonaceous (NCs) chondrites, which generally contain very rare refractory inclusions, it is still not clear to what extent CAIs and AOAs make up the Al-rich chondrule precursors in these meteorites (MacPherson and Huss, 2005). Based on bulk chemical compositions, Bischoff and Keil (1983b, 1984) defined several subtypes of Al-rich chondrules in ordinary chondrites – Na,Al-rich ($Na_2O \geq 5.0$ wt%), Ca,Al-rich ($Na_2O \leq 5.0$ wt%), Na-Cr,Al-rich ($Cr_2O_3 \geq 2.4$wt%) and intermediate.

A detailed study of the Na,Al-rich chondrules from ordinary, Rumuruti, and CO3.1 chondrites has shown that these chondrules typically consist of euhedral-to-subhedral mafic minerals embedded within a brownish nepheline-normative, glassy mesostasis and often have volatility-controlled rare earth element (REE) patterns – Group II, III, and ultra-refractory (Ebert and Bischoff, 2016) – similar to those commonly observed in CAIs (Mason and Martin, 1977; MacPherson et al., 1988; Davis et al., 2018) and AOAs (Grossmann et al., 1979). The combination of elevated refractory element abundances (Al, Ti, and REE), as well as CAI-like group II and group III REE patterns provide strong evidence that Al-rich chondrules contained refractory precursors chemically and mineralogically similar to CAIs and AOAs, providing a link between the two major chondritic components, chondrules and refractory inclusions (Ebert and Bischoff, 2016). It has to be mentioned that this connection between Al-rich chondrules and CAIs and AOAs based on the REE patterns has been questioned by Jacquet et al. (2018, 2019).

Similar connections between Al-rich chondrules and refractory material can be drawn by considering the Ti-isotope compositions. Ca,Al-rich inclusions in CCs and OCs typically have ^{50}Ti excesses between ~2−16 ε units (e.g., Trinquier et al., 2009; Williams et al., 2016; Ebert et al., 2018; Shollenberger et al., 2018; Render et al., 2019), also linking CAIs from different chondrites to a formation in a common isotopic reservoir. As titanium isotopes are not expected to exchange with the nebular gas during chondrule formation (Niemeyer, 1988a,b; Gerber et al., 2017), ^{50}Ti is a perfect tracer to constrain the role of CAI constituents as possible precursor components of Al-rich chondrules. If ^{50}Ti-enriched refractory material was involved as a precursor, it should be still detectable in the resulting chondrules. Indeed, Na,Al-rich chondrules in CO chondrites show positive excesses of ^{50}Ti up to 14.5±0.5ε, which is best explained by the presence of CAI-like material in their precursors (Ebert et al., 2018). However, Na,Al-rich chondrules in ordinary chondrites show no evidence for ^{50}Ti excesses (ε^{50}Ti range from ~ −2 to 0); these Ti-isotope compositions are similar to those of ferromagnesian chondrules and bulk ordinary chondrites (Gerber et al., 2017; Ebert et al., 2018). Based on these observations, Ebert et al. (2018) concluded that an "unknown" refractory component, mineralogically and chemically similar to known CAIs but with normal Ti-isotope compositions, was among Na,Al-rich chondrule precursors in the ordinary chondrites' chondrule-forming region. Possible explanations for such a component could be either a heterogeneous distribution of ^{50}Ti in the CAI-forming region or a different non-CAI origin of the refractory precursors.

Based on the solar-like oxygen isotopic compositions of refractory inclusions (McKeegan et al., 2011) and the presence of decay products of short-lived radionuclides ^{7}Be and ^{10}Be formed by solar energetic particle irradiation, CAIs are thought to have formed from a gas of approximately solar composition, possibly close to the young Sun, and were subsequently distributed into the different regions of the protoplanetary disk where chondrules formed and chondrites accreted (Shu et al., 1996; McKeegan et al., 2000; MacPherson et al., 2003; Brownlee et al., 2006; Chaussidon et al., 2006; Ciesla, 2007; Krot et al., 2009; Wielandt et al., 2012; MacPherson, 2014 and references therein). If CAIs or AOAs were present among Al-rich chondrule precursors, these chondrules may have preserved an ^{16}O-rich signature of these precursors. In addition, O-isotope compositions of Al-rich chondrules in ordinary chondrites can be potentially used to constrain their formation region to the inner *vs.* outer Solar System. Note that on a three-isotope oxygen diagram (δ^{17}O *vs* δ^{18}O), vast majority of chondrules in CCs plot below the terrestrial fractionation (TF) line, whereas those from NCs plot along or above it (e.g., Tenner et al., 2018 and references therein).

In this context, it is important to consider the effects of exchange and equilibration of O-isotopes during chondrule formation or during metasomatic/aqueous alteration in the solar nebula and/or on the chondrites' parent bodies. Melted chondrules behaved as open systems (e.g., Kita et al., 2010) and appear to have experienced O-isotope exchange with the surrounding solar nebula gas (e.g., Clayton et al., 1991; Tenner et al., 2018). Oxygen isotopic compositions of most CAIs, AOAs, and chondrules (except relict grains) from most unmetamorphosed (petrologic type 2−3.0) chondrites are uniform (e.g., Makide et al., 2009; Ushikubo et al., 2017; Kööp et al., 2016; Krot et al., 2017b, 2019a). This O-isotope homogeneity can be subsequently modified by post-crystallization O-isotope exchange with either nebular gas or aqueous fluid on the chondrites' parent asteroids; the latter process is consistent with the common presence of isotopically heterogeneous chondrules and refractory inclusions in metamorphosed (petrologic type >3.0) CO and CV carbonaceous chondrites (e.g., Wasson et al., 2001; Itoh et al., 2004, 2007; Rudraswami et al., 2011; Krot et al., 2019a,b; Ebert et al., 2020). To minimize the effects of parent body alteration, in this study, we used only Al-rich chondrules from the weakly metamorphosed ordinary chondrites of petrologic type ≤3.2 [NWA 3358 (H3.1), Adrar 003 (L/LL3.1), Vicencia (L3.15), Krymka (LL3.2), and Vicencia (LL3.2)] and the CO3.1 chondrite Dar al Gani (DaG) 083.

2. METHODS AND SAMPLES

All polished thin sections and meteorite chips discussed in this work were provided by the Institut für Planetologie of the Westfälische Wilhelms-Universität Münster and by the Hawai‘i Institute of Geophysics and Planetology (HIGP), University of Hawai‘i (UH) at Mānoa.

For identification of Al-rich chondrules, a Zeiss Axiophot optical microscope was used for thin sections microscopy. Thick sections and meteorite chips were studied with a JEOL 6610-LV electron microscope (SEM) at the Interdisciplinary Center for Electron Microscopy and Microanalysis (ICEM) at the Westfälische Wilhelms-Universität Münster.

Each side of twelve individual chondritic chips (two from Adrar 003, two from Krymka, two from NWA 3358, one from NWA 8580, and six from Vicencia) and one thick section from NWA 3358 were investigated by Al-elemental maps using a SEM. Not all identified Al-rich chondrules were used for further mineralogical and O-isotopic investigations because the selected Al-rich chondrules should be enriched in Na and should also be large enough (>250 µm) for further Ti-isotope measurements in a follow up work. Because, for Ti-isotope measurements, the chondrules will be extracted from the chip or the thick section using a micro

mill with a minimum drill size of 250µm. In addition, Al-rich chondrules with Na <4wt% were chosen, if they contain spinel.

Furthermore, 18 thin sections (six from Adrar 003, 3 from Krymka, 3 from NWA 3358, 2 from NWA 5206 (no Al-rich chondrule were found), 3 from Vicencia, and one from the CO3.1 chondrite DaG 083) were investigated by optical microscopy in transmitted and reflected light. We identified Al-rich chondrules by their brownish color in transmitted light and/or their distinct appearance (clear crystals in a glassy mesostasis) in transmitted light. Selected samples were further examined at the SEM and those containing spinel or olivine grains (where the optical appearance gives the possibility for a relict grain) were chosen (Table 1).

In this study, we investigated 17 Al-rich chondrules (Figs. 1-6) from five different UOCs [7 from NWA 3385 (H3.1), 3 from Adrar 003 (L/LL3.1), 3 from NWA 8580 (L3.15), 3 from Krymka (LL3.2), and 1 from Vicência (LL3.2)] and 4 Al-rich chondrules (Figs. 7 and 8) from the CO3.1 chondrite DaG 083 (Table 1). In this work, a more simplified sub-classification is used. Na-enriched Al-rich chondrules (Na_2O >4 wt%) are labeled as NaC-# and Al-rich chondrules with Na_2O <4 wt% as Ca-Al-#. If we refer to Al-rich chondrules in the text, both groups are addressed.

Quantitative mineral analyses (Table 2) were obtained using a JEOL JXA 8530F electron microprobe. For bulk and regular mineral analyses operating conditions were 15 kV accelerating voltage and a probe current of 15 nA. The measurement time for Na and K was 7 s and 3 s and for all other elements 15 s and 10 s on peak and background, respectively. Natural and synthetic reference materials were used for calibration. The matrix corrections were done according to the $\Phi\rho(z)$ procedure (Armstrong, 1991).

On selected olivine grains in various chondrules Na, Mn, Fe, Cr, and Ca concentrations were determined using a higher beam current of 100 nA and longer counting times of 350/175 s for Na, Al, Mn, 180/90 s for Cr, Ni, P, Ca. 10/5 s for Si, Mg, and Fe on peak and background, respectively (Table A1). For Na under these conditions a 3σ detection limit of ~22 ppm was achieved (Table A2). Alexander et al. (2008) showed that olivine is stable to Na loss under similar conditions. In order to check precision and accuracy over the course of this study we measured the MongOl sh11-2 reference olivine (Batanova et al., 2019) as an unknown. Obtained major and trace element compositions match within error the values given by Batanova et al. (2019). Furthermore, we analyse a synthetic forsterite to ensure true zero-count rates for all trace elements.

Oxygen-isotope analyses were carried out with the UH Cameca IMS-1280 ion microprobe using a method described by Nagashima et al. (2015). A primary Cs^+ ion beam with a beam

current of ~25 pA was focused to 1−2 µm and rastered over 2×2 µm² area. Oxygen isotopes ($^{16}O^-$, $^{17}O^-$ and $^{18}O^-$) were measured in multicollection mode on a Faraday cup and two electron multipliers, respectively. Instrumental fractionation was corrected by using terrestrial standards: San Carlos olivine for olivine and low-Ca pyroxene (Wo≤25), augite for Ca pyroxene (Wo>25), spinel for spinel, and Miyakejima anorthite for plagioclase and glassy mesostasis. Oxygen isotopic compositions of minerals and glasses in the Al-rich chondrules studied are listed in Table 3a,b and summarized in Figs. 9 and 10. Oxygen-isotope compositions are reported as $\delta^{17}O$ and $\delta^{18}O$, deviations from Vienna Standard Mean Ocean Water in parts per thousand (SMOW; $^{17}O/^{16}O_{VSMOW}$ = 0.000380; $^{18}O/^{16}O_{VSMOW}$ = 0.002005; De Laeter et al., 2003): $\delta^{17};^{18}O_{SMOW} = [(^{17,18}O/^{16}O_{sample}) / (^{17,18}O/^{16}O_{VSMOW}) - 1] * 1000$, and as deviation from the terrestrial fractionation (TF) line: $\Delta^{17}O=\delta^{17}O - 0.52 * \delta^{18}O$. The reported 2σ uncertainties include both the internal measurement precision on an individual analysis and the external reproducibility for standard measurements during a given analytical session.

The bulk compositions of selected chondrules (Table 4) were calculated based on the mineral compositions and their weighted modal proportions, determined by point counting using the analysis software JMicroVision. The following equation for the bulk composition was used from Berlin (2009):

$$(1) Element\ Z = conc_{phase\ 1}^{Element\ Z}\left[\frac{vol\%_{phase1}*\rho_{phase1}}{\sum_1^n(vol\%_{phasen}*\rho_{phasen})}\right] + \cdots + conc_{phase\ m}^{Element\ Z}\left[\frac{vol\%_{phasem}*\rho_{phasem}}{\sum_1^n(vol\%_{phasen}*\rho_{phasen})}\right]$$

Here, *conc* is the elemental composition in wt% and ρ is the density of the analyzed phase.
The density of olivine was calculated based on the fraction of forsterite (x) using the formula of Fisher and Medaris (1969):

$$(2)\ \rho_x = 4.4048 - 1.1353x - 0.0435x^2$$

The density of pyroxene was linearly interpolated between the end-member enstatite (3.2 g/cm³) and ferrosilite (3.95 g/cm³). A similar estimation was done for the Ca-rich pyroxene with the endmember diopside (3.28 g/cm³) and hedenbergite (3.56 g/cm³). Spinel is nearly pure Mg-spinel; a density of 3.59 g/cm³ was used.
Density calculations for the glass were performed using the density model from Fluegel (2007):

$$(3)\ \rho_{glass} = b_0 * \sum_{i=1}^n[b_iC_i + \sum_{k=1}^n(b_{ik}C_iC_k + \sum_{m=k}^n b_{ikm}C_iC_kC_m)]$$

Where b values are the model coefficients given in Fluegel (2007) and C values are the glass concentrations in mol%. See Fluegel (2007) for more details.

3. RESULTS

3.1 AL-RICH CHONDRULES FROM TYPE 3 ORDINARY CHONDRITES

NWA 3358 (H3.1)

NaC-1 is a porphyritic pyroxene (PP) chondrule, ~150 µm in apparent diameter (Fig. 1a). It consists of low-Ca pyroxene ($En_{94}Wo_5$) phenocrysts rimmed by Ca pyroxene ($En_{56}Wo_{43}$) and embedded in glassy mesostasis (12.2 wt% Na_2O). Oxygen-isotope compositions were measured for two low-Ca pyroxene grains in the core and rim of the chondrule, and for the mesostasis in the core. The pyroxenes and mesostasis are in O-isotope disequilibrium. Two low-Ca pyroxene grains have similar $\Delta^{17}O$, −4.3±2.8‰ and −4.5±2.5‰, and on a three-isotope oxygen diagram ($\delta^{17}O$ *vs.* $\delta^{18}O$) plot along the carbonaceous chondrite anhydrous mineral (CCAM; Clayton et al., 1977) line. Chondrule mesostasis is ^{16}O-poor ($\Delta^{17}O$ = 5.0±2.1‰).

NaC-2 is a porphyritic olivine-pyroxene (POP) chondrule, ~300 µm in apparent diameter surrounded by a rim (Fig. 1b). It is composed of skeletal crystals of forsteritic olivine (Fo_{99}) and chemically zoned pyroxenes ($En_{94}Wo_5$ - $En_{51}Wo_{48}$) embedded in glassy mesostasis (13.0 wt% Na_2O). Chondrule phenocrysts are in O-isotope disequilibrium with mesostasis. Olivine and Ca pyroxene phenocrysts have similar $\Delta^{17}O$ (−0.7±2.3‰ and −0.1±1.8‰, respectively) and plot along the TF line, whereas chondrule mesostasis is ^{16}O-depleted ($\Delta^{17}O$ ~ 4±2‰) and plots above TF line.

NaC-3 is a PO chondrule (Fig. 1c), ~160 µm in diameter, composed of skeletal olivine phenocrysts ($Fo_{99;}$ $\Delta^{17}O$ = −0.6±2.3‰) embedded in a glassy mesostasis (12.7 wt% Na_2O; $\Delta^{17}O$ = 3.3±2.0‰) and partly surrounded by a rim. The O-isotopic composition of the mesostasis is clearly resolved relative to olivine phenocrysts in a three-isotope oxygen diagram (Fig.9).

Chondrule *NaC-4*, ~340 µm in apparent diameter, has a glassy texture and contains 7.8 wt% Na_2O (Fig. 2a) and partly surrounded by a rim. Quartz is present along a crack in the lower part of the chondrule. Oxygen isotopic composition of mesostasis in the core appears to be slightly ^{16}O-enriched relative to that near the edge; the difference, however, cannot be resolved with 2σ uncertainty ($\Delta^{17}O$ = −1.6±2.1‰ and 0.6±2.1‰, respectively).

NaC-5 is a rimmed POP chondrule (Fig. 2b), ~350 µm in apparent diameter, consisting of skeletal crystals of forsteritic olivine (Fo_{99}) and igneously-zoned pyroxenes ($En_{82}Wo_{18}$ – $En_{63}Wo_{37}$) embedded in glassy mesostasis (13.9 wt% Na_2O). The chondrule has a

heterogeneous O-isotope composition visible in the three-isotope oxygen diagram, in which the glassy mesostasis ($\Delta^{17}O$ = 4.1±2.1‰) is ^{16}O depleted compared to olivine, low-Ca pyroxene, and Ca pyroxene, which have similar $\Delta^{17}O$: 0.6±2.0‰, 1.4±2.0‰, and 0.8±1.6‰, respectively.

NaC-6 is a rimmed POP chondrule (Fig. 2c), ~250 µm in apparent diameter, made of skeletal olivine (Fo_{100}) and Ca pyroxene ($En_{48}Wo_{51}$) grains embedded in glassy mesostasis (14.7 wt% Na_2O). The glassy mesostasis is ^{16}O-depleted ($\Delta^{17}O$ = 1.2±2.1‰) compared to olivine ($\Delta^{17}O$ = −4.2±2.1‰) and Ca pyroxene ($\Delta^{17}O$ = −2.3±1.6‰). On a three-isotope oxygen diagram, Ca pyroxene is displaced to the left from that of olivine, possibly as a result of improper standard (augite) used.

Ca-Al-1 is a PP chondrule (Fig. 6a), ~550 µm in apparent diameter, composed of elongated pyroxene grains ($En_{92}Wo_8$ – $En_{63}Wo_{37}$) and several rounded spinel grains all embedded in glassy mesostasis (16.2 wt% Na_2O). It is partly surrounded by a thin rim. Ca pyroxenes and spinel are ^{16}O-enriched ($\Delta^{17}O$ = −1.8±1.5‰ and −2.6±1.4‰, respectively) compared to the glassy mesostasis ($\Delta^{17}O$ = 5.6±2.2‰).

Adrar 003 (L/LL3.1)

NaC-7 is an ellipsoidal, 250×300 µm POP chondrule (Fig. 3a). Its central part consists of skeletal olivine grains (Fo_{98-99}) and a small (~3 µm) spinel grain surrounded by glassy mesostasis (13.8 wt% Na_2O). The peripheral portion is dominated by many chemically zoned pyroxenes ($En_{90}Wo_8$ – $En_{60}Wo_{38}$). The olivine, spinel, and glassy mesostasis measured for O-isotope compositions have similar (within uncertainty of our SIMS measurements) $\Delta^{17}O$ values of 0.8±1.9‰, 0.3±1.1‰, and 1.5±1.9‰, respectively.

NaC-8 is a POP chondrule (Fig. 3b), ~850×950 µm in size, composed of skeletal olivine grains (Fo_{99}), an aggregate of subhedral olivine grains (Fo_{99}), and igneously zoned pyroxenes ($En_{94}Wo_4$ – $En_{57}Wo_{41}$), all embedded in a glassy mesostasis (10.6 wt% Na_2O). Both textural types of olivine grains and the low-Ca pyroxene grain analyzed have similar $\Delta^{17}O$: −1.2±1.9‰, −1.3±2.1‰, and −0.9±1.9‰, respectively. The glassy mesostasis ($\Delta^{17}O$ = 1.3±2.2‰) cannot be resolved with 2σ uncertainty from the embedded phenocrysts.

NaC-9 is a POP chondrule (Fig. 3c), ~450 µm in apparent diameter, composed mainly of skeletal olivine grains (Fo_{99-100}) and glassy mesostasis (10.9 wt% Na_2O); small crystals of low-Ca pyroxene ($En_{95}Wo_4$) and Ca pyroxenes ($En_{53}Wo_{47}$) are concentrated in the peripheral part of the chondrule. The glassy mesostasis is ^{16}O depleted relative to olivine phenocrysts ($\Delta^{17}O$ = 1.7±2.2‰ and −2.7±1.8‰, respectively).

NWA 8580 (L3.15)

NaC-12 is a PO chondrule (Fig. 4c), ~400 µm in apparent diameter, and consists of skeletal olivine grains (Fo_{99}) embedded in glassy mesostasis (12.0 wt% Na_2O). The olivine and chondrule mesostasis have similar (within uncertainty of our SIMS measurements) $\Delta^{17}O$ values of 1.2±2.7‰ and −0.4±2.3‰, respectively.

NaC-13 is a POP chondrule (Fig. 5a), ~450×750 µm in size, and made of Ca pyroxene ($En_{56}Wo_{43}$) and olivine (Fo_{99-100}) grains embedded in glassy mesostasis (13.0 wt% Na_2O). The pyroxene and olivine grains are concentrated in the central and peripheral parts of the chondrule, respectively. The chondrule has a heterogeneous O-isotope composition: The glassy mesostasis is ^{16}O-depleted relative to olivine and Ca pyroxene ($\Delta^{17}O$ = 2.3±2.2‰, −4.5±2.2‰, and −2.2±2‰, respectively).

Ca-Al-2 is a fragmented chondrule exposed at the edge of the meteorite chip (Fig. 6b). It consists of skeletal hibonite and Ca-Al-Ti pyroxenes (25.3 wt% Al_2O_3; 4.2 wt% TiO_2), and euhedral spinel grains all embedded in glassy mesostasis. Olivine is absent. Hibonite bearing (micro-)chondules are present in different types of chondritic meteorites and they can have large isotopically anomalies as well as REEs (rare earth elements) with refractory pattern (e.g., Grossman et al., 1988; Ireland et al. 1991; Russell et al., 1998; Simon et al., 1998). Phenocrysts and glassy mesostasis in Ca-Al-2 have similar O-isotope compositions, with $\Delta^{17}O$ of ~ −2.5±1.5‰. On a three-isotope oxygen diagram, all analyses are displaced to the left from the Primitive Chondrule Mineral (PCM) line (Ushikubo et al., 2012), which may reflect IMF effects due to the location of the chondrule right on the edge of the section.

Krymka (LL3.2)

NaC-10 is a PP chondrule (Fig. 4a), ~370×500 µm in size, composed mainly of igneously zoned pyroxene crystals ($En_{98}Wo_1$ – $En_{53}Wo_{46}$) embedded in glassy mesostasis (13.2 wt% Na_2O). The only analysis obtained for the chondrule is the mesostasis with $\Delta^{17}O$ = 2.5±2.3‰.

NaC-11 is a partly rimmed PO chondrule (Fig. 4b), ~250×330 µm in size, made of skeletal olivine grains (Fo_{100}) embedded in glassy mesostasis (11.5 wt% Na_2O). Olivine ($\Delta^{17}O$ = −2.3±3.2‰) is clearly resolved to mesostasis ($\Delta^{17}O$ = 0.7±2.7‰) in a three-isotope oxygen diagram.

NaC-14 is a PO chondrule (Fig. 5b), ~350×450 µm in size, composed of coarse subhedral (Fo_{99}) and skeletal olivine (Fo_{96-98}) grains embedded in glassy mesostasis (9.1 wt% Na_2O). The coarse olivine has a similar ^{16}O composition relative to the mesostasis ($\Delta^{17}O$ = 0.6±2.1‰ and 2.3±2.1‰, respectively) but are resolved in a three-isotope oxygen diagram

Vicência (LL3.2)

Ca-Al-3 is an ellipsoidal chondrule, ~700×850 µm in size, composed mainly of coarse-grained Al-diopside and skeletal olivine crystals embedded in a glassy mesostasis (Fig. 6c). Small subhedral spinel grains occur near the chondrule edge. Two spinel grains analyzed appear to be slightly ^{16}O enriched relative to two Al-diopsides measured (Δ^{17}O = −2.4±1.2‰, −2.0±1.4‰ and −0.8±2.7‰, 0.4±2.5‰). Glassy mesostasis is the most ^{16}O-depleted phase (Δ^{17}O = 2.6±2.3‰). As this sample was included in the study in a later stage, no microprobe data of the mineralogy is present.

3.2. Al-rich chondrules from Dar al Gani 083 (CO3.1) chondrite

A POP chondrule *CO-NaC-1* (Fig. 7a), ~500×540 µm in size, consists of olivine (Fo_{99}), low-Ca pyroxene ($En_{96}Wo_3$) overgrown by Ca pyroxene ($En_{54}Wo_{45}$), and glassy mesostasis (12.9 wt% Na_2O). Olivine and low-Ca pyroxene are ^{16}O-enriched (Δ^{17}O = −6.3±2.0‰ and −7.4±1.9‰, respectively) compared to mesostasis (Δ^{17}O = −1.8±2.1‰). Ca pyroxene (Δ^{17}O = −4.3±1.8‰) cannot be resolved with 2σ uncertainty from the mesostasis.

A PP chondrule *CO-NaC-2* (Fig. 7b), ~170×200 µm in size, consists of Ca pyroxene skeletal crystals (~$En_{66}Wo_{32}$) and mesostasis containing numerous quenched crystals. Two of the pyroxenes measured have similar Δ^{17}O values of −2.8±1.9‰ and −3.6±1.5‰, respectively.

A PO chondrule *CO-Ca-Al-1* (Fig. 8a), ~1150 µm in apparent diameter, consists of rounded spinel grains and skeletal crystals of olivine (Fo_{99}) and Ca pyroxene ($En_{59}Wo_{40}$) all embedded in glassy mesostasis (3.3 wt% Na_2O). Two spinel grains measured are similarly ^{16}O-rich (Δ^{17}O ~ −24±1.4‰). Olivine, Ca pyroxene, and mesostasis have less ^{16}O-rich compositions (Δ^{17}O ~ −6±2‰, −5.5±1.7‰, and −4.5±2.0‰, respectively).

A PO chondrule *CO-Ca-Al-2* (Fig. 8b), ~190×210 µm in size, consists of skeletal spinel and olivine (Fo_{98}) grains embedded in Ca pyroxene that is not a glassy mesostasis. All phases have similar (within uncertainty of our SIMS measurements) Δ^{17}O values (spinel: −2.2±1.6‰, olivine: −1.0±2.0‰, and Ca pyroxene: −0.3±2.1‰, respectively) and plot on the PCM line.

3.3. Bulk composition and precise Na measurements from selected Al-rich chondrules

We performed more detailed and precise element measurements within selected olivine grains and bulk calculations for five different Al-rich chondrules (Table A3). Except for CO-Ca-Al-1, all Na-Al-rich chondrule glasses have Na_2O >13.0 wt% (Table 4 and Table A3 for all

Al-rich chondrules) and a calculated bulk Na_2O value >4.0 wt% (Table 4). Measurement and calculation follow the method of Alexander et al. (2008). K_D rim was calculated based on the measured Na values of the chondrule mesostasis and the highest Na-value measured which is closest to the olivine rim and also unaffected by the surrounding glass. The K_D core is calculated by the lowest Na value in the center of the olivine grain in relationship to the chondrule bulk composition. The ratios of K_D rim/ K_D core in chondrule olivines were 0.9303-1.9593, plotting around the 1:1 line (Fig. 11). In general, the Na_2O distribution within one olivine grain does not show high variability, except directly on the rim itself (Fig. 12; Table A4).

4. DISCUSSION

4.1. AL-RICH CHONDRULES FROM A CO-CHONDRITE

Four Al-rich chondrules from the CO3.1 chondrite Dar al Gani 083 were measured for O-isotope compositions (Figs. 7, 8, 10; Table 3b). The chondrule *CO-Ca-Al-2* has an internally uniform O-isotope composition, with spinel, olivine, and Ca pyroxene having $\Delta^{17}O$ values of −2, −1, and 0‰, respectively. In chondrule *CO-NaC-2*, only Ca pyroxene grains were measured ($\Delta^{17}O \sim -3$‰). Two other chondrules, *CO-Ca-Al-1* and *CO-NaC-1*, are isotopically heterogeneous, with $\Delta^{17}O$ ranging from ~ −25 to ~ −4‰ and from ~ −7 to −2‰, respectively. In *CO-Ca-Al-1*, this heterogeneity is due to the presence of ^{16}O-rich spinel grains, which are probably relicts; olivine, Ca pyroxene, and glassy mesostasis have similar (within uncertainty of our SIMS measurements) $\Delta^{17}O$ values of −6, −6 and −4.5‰, respectively. In *CO-NaC-1*, the heterogeneity is due to ^{16}O-depleted composition of mesostasis ($\Delta^{17}O \sim -2$‰) compared to olivine and low-Ca pyroxene which have similar $\Delta^{17}O$ values of −6 and −7 respectively. The Ca pyroxene cannot be resolved with 2σ uncertainty from the mesostasis but is clearly resolved in the three-isotope oxygen diagram.

Oxygen-isotope compositions of relict spinel grains in *CO-Ca-Al-1* are similar to those in CAIs and AOAs in CO3.0 chondrites (Itoh et al., 2004; Krot, 2019), indicating the presence of the CAI- or AOA-like precursors in *CO-Ca-Al-1*. A similar conclusion was reached by Chaumard et al. (2018), Marrocchi et al. (2018, 2019) and Zhang et al. (2020), based on the presence of ^{16}O-rich relict spinel and forsterite grains in Al-rich and ferromagnesian chondrules from CV and CM chondrites. Therefore, the ^{16}O-enriched refractory material – most likely constituents of former CAIs and AOAs − was among the precursors for chondrules in general in CV, CM, and CO chondrites.

Oxygen-isotope compositions of the Al-rich chondrule phenocrysts are not systematically ^{16}O-enriched relative to those in ferromagnesian chondrules from CO chondrite (Fig. 10), suggesting significant O-isotope exchange of chondrule melt with the surrounding nebular gas that nearly completely erased the ^{16}O-rich signature of CAI- and/or AOA-like precursors.

Chondrule phenocrysts and mesostases in chondrules from the carbonaceous chondrite Acfer 094 (C3.00) have homogenous O-isotope compositions (Ushikubo et al., 2012). In contrast, themesostasis in the investigated Al-rich chondrule CO-NaC-1 from Dar al Gani 083 (CO3.1) appears to be ^{16}O depleted relative to chondrule phenocrysts (Fig. 10c); which approach Δ^{17}O value of aqueously formed fayalite and magnetite of -1.6±0.9‰ for CO chondrites reported by Doyle et al. (2015). Therefore, we infer that this O-isotope heterogeneity is most likely due to post-crystallization O-isotope exchange with an aqueous fluid on the CO parent asteroid, which could have occurred at ~200−300°C (Doyle et al., 2015). Oxygen-isotope exchange with an aqueous fluid has also been previously inferred for melilite, grossite, krotite, and Zr,Sc-rich oxides and silicates in isotopically heterogeneous CAIs from metamorphosed CO chondrites (Wasson et al., 2001; Krot et al., 2019a).

4.2. AL-RICH CHONDRULES FROM ORDINARY CHONDRITES

Contrary to the CO Al-rich chondrules, the Al-rich chondrules from ordinary chondrites generally do not fall on the PCM/CCAM line and instead scatter in a much larger region between the TFL and CCAM line in a three-isotope oxygen diagram (Fig. 9). Therefore, the situation in the case of Al-rich chondrules from ordinary chondrites is more complex than for Al-rich chondrules from DaG 083.

4.2.1. Heterogeneity and ^{18}O-depletion within different phenocrysts

The O-isotopic composition of phenocrysts within ordinary chondrites' Al-rich chondrules is much more spread out between the TFL and CCAM line compared to that of the Al-rich chondrules from CO chondrites (Figs. 9 and 10). A similar spread for phenocrysts within Al-rich chondrules from ordinary chondrites was reported by Russell et al. (2000). Since the investigated objects from Russell et al. (2000) are from chondrites of petrologic type 3.4, it cannot be excluded that the slight shift to the left of the PCM line is caused by a mild thermal metamorphism with the present of a fluid on the ordinary chondrite parent body (Krot et al., 2006b). However, spinel, olivine, and Ca pyroxene in CAIs and AOAs from NWA 3358 (H3.1) do not show effects of parent body alteration, and they still have their pristine O-isotopic composition (Ebert et al., 2020). Thus, the O-isotopic composition of spinel, olivine, and Ca pyroxene in the investigated Al-rich chondrules (from type ≤3.1) should be also unaffected by

alteration processes in the solar nebula or on the parent body, and the shift to the left of the PCM line must have a different origin.

If the spread to the left of the PCM line is caused by a unique O-isotopic composition of the refractory precursor material, the phenocrysts within a single chondrule should have similar O-isotopic compositions and plot close together in the three-isotope oxygen diagram. However, this is not the case, and the O-isotopic composition depends on the mineral phase, where Ca pyroxenes are, in general, depleted in ^{18}O and compared to olivines, low-Ca pyroxenes, and spinels (Fig. 9c). A possible shift in the O-isotopic composition of the chondrule melt's during chondrule formation could lead to a heterogenous O-isotopic composition within a single chondrule (Piralla et al., 2021). However, this scenario seems to be unlikely in this case because: (i) it is assumed that Al-rich chondrule cooled very fast (Ebert and Bischoff, 2016), (ii) the time window between crystallization of olivine, low-Ca pyroxene and Ca pyroxene is short (iii) the change in O-isotopic composition should have happened in every Al-rich chondrule just before and only when Ca-pyroxene crystallized, and (iv) no other mineral phases were affected. Therefore, we assume that in this case, the shift to an ^{18}O-depleted composition for Ca pyroxenes is most likely caused by a different mineral composition of the used standard (augite) and the measured Ca pyroxenes and/or unknown instrumental reasons. This is also visible in Al-rich chondrules from CO chondrites, where Ca pyroxenes are also slightly shifted to the left of the CCAM line (Fig. 10). Therefore, only the position of olivines, spinels, and low-Ca pyroxenes can be used in the three-isotope oxygen diagram to make statements about the Al-rich chondrule precursor material. These mineral phases plot along the PCM and Young and Russell (1998) (Y&R) line, similar to the Al-rich chondrules from CO chondrites.

Exceptions are the phenocrysts (hibonite, spinel, Al-rich diopside) from Ca-Al-2, which are also depleted in ^{18}O and, especially in the case of spinel, a shift to the left cannot be caused by matrix effects during the measurements.

Unfortunately, the location of this hibonite-bearing Al-rich chondrule is directly at the edge of the meteorite chip (Fig. 6a), and the measurements can be affected by huge topographic effects. Such topographic effects can result in large analytical uncertainties and in a decrease in ^{18}O up to 5‰ (Kita et al., 2009). For example, a hypothetical increase of ^{18}O of 3–4‰ would shift the phenocryst between the PCM and Y&R lines on the three-isotope oxygen diagram. Nevertheless, the phenocrysts in Ca-Al-2 are enriched in ^{16}O and clearly differ in their oxygen isotope composition from bulk ordinary chondrites and ferromagnesian chondrules.

A mixing line through the remaining phenocryst (without Ca-Al-2 and Ca pyroxenes) would create a line with a slope of ~0.99, which is very similar to the Y&R and PCM lines.

Therefore, we assume that the O-isotope composition of the ^{16}O-enriched refractory component of the Al-rich chondrule precursor follows the PCM and Y&R lines and were mixed with the ^{16}O-depleted material from the ordinary chondrite region. Some phenocrysts avoided complete equilibration with the solar gas during the chondrule formation event and still preserve a ^{16}O-enriched composition up to $\Delta^{17}O$ = -4.5 ±2.2‰ (this study) and up to $\Delta^{17}O$ = -6.1 ±2.8‰ (Russell et al., 2000), which differ significantly from the oxygen isotopic composition of bulk ordinary chondrites ($\Delta^{17}O$ = 0.7 – 1.3‰; Clayton et al., 1991) and bulk Fe,Mg chondrules ($\Delta^{17}O$ = 0.0 – 1.7‰; e.g., Clayton et al., 1991; Kita et al., 2010; Metzler and Pack, 2016). This stands in contrast to the ^{50}Ti data which are undistinguishable from those of Fe,Mg chondrules and bulk ordinary chondrites (Ebert et al., 2018).

4.2.2. Origin of the refractory material for the Al-rich chondrules

No relict grains with an excess in ^{16}O (similar to the relict grains in CO-Ca-Al-1) were present within the ordinary chondrite Al-rich chondrules studied, and the original oxygen isotopic composition of a possible refractory precursor remains unknown.

In order to be able to make inferences about the origin of the refractory precursor material, we have summarized the key facts we know about the Al-rich chondrules from ordinary chondrites.

(1) Al-rich chondrules differ compositionally from ferromagnesian chondrules mainly by higher Al_2O_3 (>10 wt%), $CaO+Na_2O$, and TiO_2 and lower MgO concentrations (e.g., Bischoff and Keil, 1983, 1984; Krot and Rubin, 1994; MacPherson and Huss, 2005; Ebert and Bischoff, 2016).

(2) Al-rich chondrules are enriched in REEs (up to >10×CI) group II, group III, and ultra-refractory REE bulk patterns that frequently show a negative anomaly in Sm (Ebert and Bischoff, 2016; Zhang et al., 2020).

(3) Al-rich chondrules show no excess in ^{50}Ti and are indistinguishable in Ti-isotope compositions from ferromagnesian chondrules and bulk ordinary chondrites. This stands in contrast to CAIs from ordinary, CV, and CO chondrites as well as to Al-rich chondrules from CO chondrites which have an excess in ^{50}Ti (Gerber et al., 2017; Ebert et al., 2018).

(4) Many Al-rich chondrules' phenocrysts are enriched in ^{16}O, and olivine and spinel in particular follow the PCM and Y&R lines in a three-isotope oxygen diagram. (Russell et al., 2000; this study).

Al-rich chondrules from ordinary chondrites are enriched in ^{16}O up to $\Delta^{17}O$ = -6.1 ±2.8‰ (Russell et al., 2000; this study), suggesting that the ordinary chondrite formation region is not the formation region for the refractory precursor material. However, no chronological information about the investigated Al-rich chondrules are available and it cannot be excluded that they were formed early in an evolving ordinary chondrite region were the O-isotopic signature could have changed from ^{16}O-rich (~-5‰) to ^{16}O-poor (~1‰) with time (Piralla et al., 2021). But previous Al-Mg studies on Al-rich chondrules in unequilibrated ordinary chondrites (Huss et al., 2001) reveal no significant differences in formation ages to Fe-Mg chondrules from ordinary chondrites (e.g., Kita et al., 2000; Pape et al. 2019).

Therefore, if we assume a similar age of origin in the examined Al-rich chondrules it is more likely that refractory material was transported to the ordinary chondrite formation region from an ^{16}O-enriched region. Similar to the precursors for Al-rich chondrules in CO and CV chondrites, but it cannot have been isotopically similar material since the Na,Al-rich chondrules in ordinary chondrites do not have an excess in ^{50}Ti (Ebert et al., 2018), whereas Al-rich chondrules from CV and CO do have an excess in ^{50}Ti (Gerber et al., 2017; Ebert et al., 2018). This stands in contrast to the isotopically similar CAIs and AOAs in non-carbonaceous and carbonaceous chondrites, which are enriched in ^{50}Ti (Ebert et al., 2018). From the more than 100 CAIs and AOAs investigated, none has been found in carbonaceous chondrites so far without an excess in ^{50}Ti (Niemeyer and Lugmair, 1981; Niederer et al., 1981; Niemeyer, 1988b; Leya et al., 2009; Trinquier et al., 2009; Williams et al., 2016; Davis et al., 2018; Ebert et al. 2018; Burkhardt et al., 2019; Render et al., 2019). Thus, it is possible that the refractory material with an excess in ^{16}O and without an excess in ^{50}Ti was exclusively present in the ordinary chondrite formation region or within the entire non-carbonaceous chondrite formation regions.

Such a unique distribution and separation of refractory material would be hard to explain with, e.g., the X-wind or disc-wind models (Shu et al., 1996; Liffman et al., 2016), because refractory inclusions without an excess in ^{50}Ti should then also be present in the CC region. However, the model about a viscous expanding disc (Nanne et al., 2019; Burkhardt et al., 2019; Brennecka et al., 2020; Kruijer et al., 2020) predicts refractory material with a different isotopic composition in the NC region (Jacquet et al., 2019). It is possible that the formation of refractory material up to 1 AU from the young Sun occurred over several hundred thousand years (Ciesla, 2010; Yang and Ciesla, 2012) and that this could create a hypothetical late formed refractory material with an excess in ^{16}O (maybe lower than in “known” CAIs) and without an excess in

^{50}Ti. Based on the model about a viscous disc, this isotopically different material (no excess in ^{50}Ti) could be exclusively present in the inner part of the solar disc and not in the CC region.

To avoid a later mixing and complete homogenization of the CC and NC regions, the material transport, especially from the outer to the inner region of the solar disc, had to be blocked or hampered. An early formation of a large planet (maybe Jupiter) could isolate both regions and prevent material exchange between them (Warren, 2011; Budde et al., 2016; van Kooten et al., 2016; Nanne et al., 2019; Burkhardt et al., 2019; Kruijer et al., 2017, 2020). Al-rich chondrules suggest that this large-scale isotopic dichotomy seen between the inner region and the outer region is not only visible in bulk meteorites, but it is also visible in their components. However, measured CAIs and AOAs in non-carbonaceous chondrites have an excess ^{50}Ti and ^{16}O (McKeegan et al., 1998; Itoh et al., 2007; Russell et al., 2016; Ebert et al., 2018, 2020). One explanation for the presence of ^{50}Ti enriched CAIs and AOAs in the NC region is that smaller inward-moving particles were able to bridge the gap created by e.g. Jupiter and larger particles were filtered out (Ebert et al., 2018; Weber et al., 2018; Haugbølle et al., 2019).

To prove this hypothesis of an exclusive refractory material in the NC chondrite region, such a unique refractory inclusion has to be found and directly investigated. Particularly challenging is that these refractory inclusions will not be different from known CAIs and AOAs in their mineralogical and, potentially, in their oxygen isotopic composition. So far, only Ti-isotope measurements can help to distinguish them from “normal” refractory material.

4.2.3. Effects of secondary alteration processes

Most of the Al-rich chondrules from ordinary chondrites have a heterogeneous O-isotopic composition of their mineral phases with Δ^{17}O values ranging from −4.5 to +5.8‰ (Fig. 9e). In general, chondrule glasses are ^{16}O-depleted relative to chondrule phenocrysts (Fig. 9b). This ^{16}O-depletion occurred after the formation of the chondrules and was caused by a secondary process like an exchange with solar gas or by alteration on the parent body; otherwise, the glass would be in equilibrium with the phenocrysts. The Δ^{17}O values of numerous chondrule glasses are similar to those of fayalite and magnetite from H, L, and LL chondrites (Choi et al., 1998; Doyle et al., 2015; Ebert et al., 2020) and plot above the ordinary chondrite bulk composition of Δ^{17}O =~+1‰ (Clayton et al., 1991). Nearly pure fayalite and magnetite are seen as low-temperature products of an aqueous fluid on the ordinary parent body, and their Δ^{17}O, ~+5‰, reflects the O-isotopic composition of this fluid (e.g., Doyle et al., 2015). In this context, Ebert et al. (2020) showed that melilite and anorthite underwent O-isotopic exchange with the fluid on the H-chondritic parent body, whereas olivine, pyroxene, spinel, and hibonite remained

unaffected. It is a logical consequence that glass with a high oxygen diffusion rate (Ryerson and McKeegan, 1994) would therefore undergo a strong O-isotopic exchange with the fluid toward complete equilibrium. Similar inferences were done by Kita et al. (2010) from O-isotope measurements of glasses in chondrules from low petrologic type (≤3.2) LL chondrites and by Zhang et al. (2014) from Al-rich chondrules in the ungrouped C3 chondrite Dar al Gani 978. The chondrule glasses are also systematically higher in $\Delta^{17}O$ compared to values for the coexisting chondrule phenocrysts (Kita et al., 2010; Zhang et al., 2014). One ferromagnesian chondrule glass from Semarkona (LL3.0) even plots on the fractionation line defined by Semarkona magnetite (Kita et al., 2010).

However, not all glasses from the Al-rich chondrules reached complete equilibrium with the fluid on their parent body. Many are still enriched in ^{16}O compared to the O-isotopic composition of magnetite and fayalite from ordinary chondrites. One reason could be that an aqueous fluid is heterogeneously distributed within the matrix and can vary from sample to sample from distinct chondrites (Dobrică and Brearley, 2020), and this will create variation in the degree of aqueous alteration between each chondrule. This is also visible in the H3.1 chondrite NWA 3358, where fayalite and sulfide laths are heterogeneously distributed within the matrix (Ebert et al., 2020). This could also be an explanation for the varying $\Delta^{17}O$ compositions of the glasses from different chondrules within the H3.1 chondrite NWA 3358 (Fig. 9e) where NaC-1, NaC-2, NaC-3, NaC-5, and Ca-Al-1 reached equilibrium with the fluid. However, glasses from Adrar (L/LL 3.10), NWA 8580 (L3.15) or Krymka (LL3.2) are also depleted in ^{16}O compared to their phenocrysts, but their O-isotopic compositions are more similar to the O-isotopic compositions of the bulk host chondrite or bulk ferromagnesian chondrules, and none of them plot in the field of magnetite and fayalite (Fig. 9f). It seems that the presence of fluid could be more important than the petrologic type of the host meteorite. This is in agreement with Dyl et al. (2012) who shows that water had a severe effect on the equilibration process of parent body constituents.

During this alteration process on the parent body, Ca could have been removed from the glass perhaps creating a Ca-enriched rim around the chondrule itself (Fig. 13a, b). NaC-2 has a clearly visible fine-grained rim around the chondrule that is enriched in Ca, and the glass has a similar O-isotope composition as fayalite from the host meteorite. In contrast, Ca-Al-2 has a homogenous O-isotopic composition and shows no clear Ca-rim around the chondrule, and this glass has a similar O-isotopic composition as the embedded phenocryst. Such a process can lead to bleached chondrules which show strong zoning and a porous and recrystallized mesostasis (Grossman et al., 2000) which is not visible in the examined chondrules. However,

in ordinary chondrites of low petrological type, aqueous alteration can leach out Ca without devitrification of the glass itself (Grossman et al., 2002). Therefore, the O-isotopic heterogeneity between the glassy mesostasis and phenocrysts within single Al-rich chondrules is most likely due to alteration processes on the ordinary parent body and supported by the presence of an aqueous fluid.

4.2.4. Origin of sodium within the Al-rich chondrules.

As refractory material seems to be a major part of Al-rich chondrules, the high Na_2O bulk composition (up to 15.2wt% Na_2O; Ebert and Bischoff, 2016) of Na-Al-rich chondrules is quite astonishing because Na is a moderately volatile element with a 50% condensation temperature (T_{50}) of ~685°C – 762°C (Lodders et al., 2009; Wood et al., 2019) and the chondrule peak temperature during chondrule formation can rise up to ~1800 – 2000°C (Jones et al., 2018). In the special case of Al-rich chondrules, heating experiments suggest that the peak temperature was between 1400 – 1500°C (Tronche et al., 2007), which is still far above the T_{50} condensation temperature of Na. Various attempts were made to explain the high Na content within the chondrule glasses, which can be grouped in open system models and closed system models. Here a very brief summary:

Alkalis (e.g., Na and K) in chondrule glasses behave as an open system with the surrounding matrix at the parent body (e.g. Grossman and Brearley, 2005), and this may explain some of the enrichment within the Na-Al-rich chondrules (Krot et al., 2018). Furthermore, it was experimentally shown that during chondrule formation under high total Na partial pressure, the resulting melt could gain a bulk Na_2O composition up to 15 wt% (Mathieu et al., 2011), which would fit very well to measured values from Na-Al-rich chondrules. Therefore, this model is proposing that the Na-Al-rich chondrules' precursor was originally free of Na, and the Na-Al-rich chondrules received Na during or after chondrule formation.

In contrast to an open system stands the idea of a closed system, in which Na was part of the chondrule precursor and was preserved in the chondrule melt during the chondrule formation process. A possible explanation could be that the CAIs' melilite altered to, e.g., nepheline and sodalite in the solar nebula (MacPherson and Huss, 2005; Ebert and Bischoff, 2016). Such a Na-enriched precursor would have to be molten, during the chondrule formation process, in a region with high Na partial pressure created by, e.g., evaporation of dust-rich regions (e.g., Cuzzi and Alexander, 2006; Alexander et al., 2008) or in a Na-enriched

atmosphere of a planetary body (Morris et al., 2012; Herbst and Greenwood, 2016) to prevent Na loss during the chondrule formation.

It is estimated that olivine crystallized throughout most of the chondrule cooling time (Ebel and Grossman, 2000) and therefore, olivine should record any changes in the Na content of the chondrule melt. Alexander et al. (2008) and Borisov et al. (2008) measured the Na content of various Fe-Mg chondrules' olivines from the LL3.0 Semarkona meteorite and concluded a closed system with regard to Na.

We adopted their method in this study for four Na-Al-rich chondrules and one Ca-Al-rich chondrule (see chapter: "Methods and Samples") and calculated Na K_D core and Na K_D rim values for ten different olivine grains (Table 4). Similar to Alexander et al. (2008), the various olivine grains plot close to a 1:1 line in a K_D core *vs.* K_D rim diagram (Fig. 11). Therefore, the Na content in the melt did not change much during the crystallization of the olivine grains. Otherwise, there would be a significant shift to the right of the 1:1 line if the melt lost a high amount of Na after the core of the olivine grains crystallized, or there would be a significant shift to the left if a high amount of Na entered the melt during the crystallization. That the Na content stayed more or less constant during the olivine crystallization is also supported by a very smooth Na trend through the single grains (Fig. 12). These results imply that the Na was either present from the beginning in the precursor or obtained by the chondrule melt after the crystallization of olivine (in the solar nebula or on the parent body) which is in agreement to previous work on Semarkona Fe,Mg chondrules (Alexander et al., 2008; Borisov et al., 2008).

It is not possible to distinguish alone with this dataset between the various ideas about the origin of the Na within the Na-Al-rich chondrules because they all have open questions that have still to be answered.

- If the Na enrichment in the glass was caused by fluid-assisted thermal metamorphism or fluid assisted percolation (Kerraouch et al., 2019), similar Na contents of various Al-rich chondrules' glasses within one thin section – without signs of brecciation – would be expected. However, in the CO3 chondrite DaG083, the Al-rich chondrules' glasses have very different Na_2O contents (CO-NaC-1 = 12.9 wt% and CO-Ca-Al-1 = 3.3 wt%). Maybe this could be explained by a heterogeneous distribution of the aqueous fluid within one meteorite sample (Dobrică and Brearley, 2020).
- If Na condensed into the chondrule melt during chondrule formation, the olivines should show differences between the K_D rim and the K_D core because it is estimated that olivine crystallized throughout much of the chondrule cooling time (Ebel and Grossman, 2000). Therefore, the crystallization of olivine had to be finished before the

Na entered the melt. Maybe a two-stage cooling scenario with a slower cooling at the beginning and very fast cooling afterward may solve the problem. This could also lead to pure forsterite with only minor Fe at the rims and the presence of the high abundances of glass.

- If Na was part of the precursor, there should be nepheline- and/or sodalite-rich refractory inclusions within type 3.0 chondrites, but this is not the case. Yet, refractory inclusions like CAIs in chondrites with a higher degree of metamorphism contain nepheline and/or sodalite, and it appears that the replacement of melilite and anorthite by Na-rich phases is an asteroidal process (Tomeoka and Itoh, 2004; Brearley and Krot, 2012). Furthermore, this would imply a closed system for the chondrule formation process regarding Na. This stands in contrast to e.g. O (Kita et al., 2010) and Si (Nagahara et al., 2008) which show exchange between the chondrule melt with the solar nebula during the chondrule formation process (Nagahara et al., 2008; Kita et al., 2010; Piralla et al., 2021).

To summarize, even though the Na measurements of olivine grains within the Na-Al-rich chondrules could also hint at a closed system, the origin of the Na remains an open question.

5. CONCLUSIONS

We investigated the mineralogy, petrology, and O-isotope compositions of 17 Al-rich chondrules and/or their constituents from unequilibrated ordinary chondrites (petrologic type <3.2) and 4 Al-rich chondrules from the CO3.1 chondrite Dar al Gani 083.

- Precise Na measurements within olivine grains of selected Al-rich chondrules reveal no changes in the chondrule melts' Na content during the olivine crystallization.
- Al-rich chondrules from the CO3.1 chondrite have a heterogeneous oxygen isotopic composition with $\Delta^{17}O$ values ranging from −24.6 to -0.3 ‰. Relict spinel grains with $\Delta^{17}O$ values of −24.6±1.3‰ prove that CAI/AOA-like material was present within the precursors for Al-rich chondrules from CO chondrites. This is well in agreement with conclusions based on ^{50}Ti investigations from Ebert et al. (2018). Besides the relict grains, Al-rich chondrules' oxygen isotopic compositions are indistinguishable from ferromagnesian chondrules from CO chondrites, supporting the idea that Al-

rich chondrules were formed, like the ferromagnesian chondrules, in the CO formation region.

- Al-rich chondrules from ordinary chondrites have also a heterogeneous oxygen isotopic composition with $\Delta^{17}O$ values ranging from −4.5 to +5.8‰, but no relict grain as ^{16}O-enriched as CAIs are present. Their heterogeneity is mineralogically controlled, where glass is, in general, depleted in ^{16}O compared to chondrules' phenocrysts, which themselves have a homogeneous oxygen isotopic composition. The ^{16}O-depletion in glass most likely results from aqueous fluid-rock interaction on their parent chondrite bodies.
- Some Al-rich chondrule phenocrysts in ordinary chondrites are indistinguishable from ferromagnesian chondrules in their oxygen isotopic composition of the constituents. They were most likely formed within the ordinary chondrite region similar to the ferromagnesian chondrules.
- Based on the ^{16}O-enriched composition of many phenocrysts within the Al-rich chondrules, the ordinary chondrite formation region seems to be unlikely the formation region for the refractory chondrule precursor material.
- The model about a viscous expanding disc can explain refractory material with a so far unknown excess in ^{16}O, but with no excess in ^{50}Ti, which is exclusively present in the ordinary chondrite accretion region and not in the CO chondrite formation region.

ACKNOWLEDGEMENTS:

We thank Ulla Heitmann (Münster) for sample preparation, Thorsten Grund for the technical assistance on the SEM, and Celeste Brennecka for writing support. We thank Gary Huss for the fruitful discussions. Furthermore, we thank Sarah Russell, Kohei Fukuda and one anonymous reviewer who provided fruitful reviews of the manuscript as well as Yves Marrocchi for his careful editorial handling. This work was funded by the Deutsche Forschungsgemeinschaft (DFG, German Research Foundation) - project numbers 413893359, 263649064, and 463342295.

REFERENCES

Alexander C. M. O'D., Grossmann J. N., Ebel D. S. and Ciesla F. J. (2008) The formation conditions of chondrules and chondrites. *Science* 320, 1617-1619.

Armstrong J. T. (1991) Quantitative elemental analysis of individual microparticles with electron beam instruments. In *Electron Probe Quantitation*. Edited by. K. F. J. Heinrich and D. E. Newbury. Plenum Press, New York, pp. 261–315.

Batanvoa V., Thompson J. M., Danyushevsky L. V., Portnyagin M. V., Garbe-Schönberg D., Hauri E., Kimura J.-I., Chang Q., Senda R., Goemann K., Chauvel C., Campillo S., Ionov D. A. and Sobolev A. V. (2019) New olivine reference material for in situ microanalysis. *Geostandards and Geoanalytical Research* 43, 453-473.

Bischoff A. and Keil K. (1983a) Ca-Al-rich chondrules and inclusions in ordinary chondrites. *Nature* 303, 588−592.

Bischoff A. and Keil K. (1983b) Catalog of Al-rich chondrules, inclusions and fragments in ordinary chondrites. Special Publication No. 22, UNM, Institute of Meteoritics, Albuquerque, pp. 1−33.

Bischoff A. and Keil K. (1984) Al-rich objects in ordinary chondrites: Related origin of carbonaceous and ordinary chondrites and their constituents. *Geochim. Cosmochim. Acta Geochim. Cosmochim. Acta* 48, 693−709.

Bischoff A., Keil K. and Stöffler D. (1985) Perovskite-hibonite-spinel-bearing inclusions and Al-rich chondrules and fragments in enstatite chondrites. *Chemie Erde* 44, 97−106.

Bischoff A., Palme H. and Spettel B. (1989) Al-rich chondrules from the Ybbsitz H4 chondrite: Evidence for formation by collision and splashing. *Earth Planet Sci. Lett.Earth Planet Sci. Lett.* 93, 170−180.

Borisov A., Pack A., Kropf A. and Palme H. (2008) Partitioning of Na between olivine and melt: An experimental study with application to the formation of meteoritic Na_2O-rich chondrule glass and refractory forsterite grains. *Geochim. Cosmochim. Acta Geochim. Cosmochim. Acta* 72, 5558-5573.

Brearley A. J. and Krot A. N. Metasomatism in the early system: The record from condritic meteorites. In *Metasomatism and the chemical transformation of rock – Lecture notes in Earth system sciences*. Edited by D. Harlov and H. Austrheim. New York, NY, Springer, pp. 659-789.

Brennecka G. A., Burkhardt C., Budde G., Kruijer T., Nimmo F. and Kleine T. (2020) Astronomical context of Solar System formation from molybdenum isotopes in meteorite inclusions. *Science* 370, 837-840.

Brownlee D. et al., (2006) Comet 81P/Wild 2 under a microscope. *Science* 314, 1711−1716.

Budde G., Burkhardt C., Brennecka G. A., Fischer-Gödde M., Kruijer T. S. and Kleine T. (2016) Molybdenum isotopic evidence for the origin of chondrules and a distinct genetic heritage of carbonaceous and non-carbonaceous meteorites. *Earth Planet Sci. Lett.Earth Planet Sci. Lett.* 454, 293−303.

Burkhardt C., Dauphas N., Hans U., Bourdon B. and Kleine T. (2019) Elemental and isotopic variability in solar system materials by mixing and processing of primordial disk reservoirs. *Geochim. Cosmochim. Acta Geochim. Cosmochim. Acta* 261, 145−170.

Chaumard N. L., Defouilloy C. and Kita N. T. (2018) Oxygen isotope systematics of chondrules in the Murchison CM2 chondrite and implications for the CO-CM relationship. *Geochim. Cosmochim. Acta Geochim. Cosmochim. Acta* 228, 220–242.

Chaussidon M., Robert F. and McKeegan K. D. (2006) Li and Be isotopic variations in an Allende CAI: Evidence for the in situ decay of short-lived ^{10}Be and for the possible presence of the short-lived nuclide ^{7}Be in the early solar system. *Geochim. Cosmochim. Acta Geochim. Cosmochim. Acta* 70, 224−245.

Choi B. G., McKeegan K. D., Krot A. N. and Wasson J. T. (1998) Extreme oxygen-isotope compositions in magnetite from unequilibrated ordinary chondrites. *Nature* 392, 577−579.

Ciesla, F. J. (2007) Outward transport of high-temperature materials around the midplane of the solar nebula. *Science* 318, 613−615.

Ciesla F. J. (2010) The distribution and ages of refractory objects in the solar nebula. *Icarus* 208, 455−467.

Clayton R. N. and Mayeda T. K. (1999) Oxygen isotope studies of carbonaceous chondrites. *Geochim. Cosmochim. Acta* 63, 2089−2104.

Clayton R. N., Onuma N., Grossman L. and Mayeda T. K. (1977). Distribution of the pre-solar component in Allende and other carbonaceous chondrites. *Earth Planet Sci. Lett.Earth Planet Sci. Lett.* 34, 209−224.

Clayton R. N., Mayeda T. K., Goswami J. N. and Olsen E. J. (1991) Oxygen isotope studies of ordinary chondrites. *Geochim. Cosmochim. Acta* 55, 2317−2337.

Cuzzi J. N. and Alexander C. M. O'D. (2006) Chondrule formation in particle-rich nebular regions at least hundreds of kilometers across. *Nature* 441, 483-485.

Davis A. M., Zhang J., Greber N. D., Hu J., Tissot F. J. H. and Dauphas N. (2018) Titanium isotopes and rare earth patterns in CAIs: Evidence for thermal processing and gas-dust decoupling in the protoplanetary disk. *Geochim. Cosmochim. Acta* 221, 275−295.

De Laeter J. R., Böhlke J. K., De Biévre P., Hidaka H., Peiser H. S., Rosman K. J. R. and Taylor P. D. P. (2003) Atomic weights of the elements. Review 2000 (IUPAC Technical Report). *Pure Appl. Chem.* 75, 683–800.

Dobrică E. and Brearley A. J. (2020) Amorphous silicates in the matrix of Semarkona: The first evidence for the localized preservation of pristine matrix materials in the most unequilibrated ordinary chondrites. *Meteorit. Planet. Sci.* 55, 649−668.

Doyle P. M., Jogo K., Nagashima K., Krot A. N., Wakita S., Ciesla F. J. and Hutcheon I. D. (2015) Early aqueous activity on the carbonaceous and ordinary chondrite parent asteroids recorded by secondary fayalite. *Nature Communications* 6, 1–10.

Dyl K. A., Bischoff A., Young E. D., Wimmer K. and Bland P. A. (2012) Early Solar System hydrothermal activity in chondritic asteroids on 1-10-year timescales. *Proc. Natl. Acad. Sci.* 109, 18306−18311.

Ebel D. S. and Grossman L. (2000) Condensation in dust-enriched systems. *Geochim. Cosmochim. Acta* 64, 339-366.

*Meteorit. Planet. Sci.*Ebert S. and Bischoff A. (2016) Genetic relationship between Na-rich chondrules and Ca,Al-rich inclusions? – Formation of Na-rich chondrules by melting of refractory and volatile precursors in the solar nebula. *Geochim. Cosmochim. Acta* 177, 182−204.

*Meteorit. Planet. Sci.Meteorit. Planet. Sci.*Ebert S., Render J., Brennecka G. A., Burkhardt C., Bischoff A., Gerber S. and Kleine T. (2018) Ti isotopic evidence for a non-CAI refractory component in the inner Solar System. *Earth Planet Sci. Lett.* 498, 257−265.

Ebert S., Bischoff A. and Krot A. N. (2019) (Na-)Al-rich chondrules and Ca,Al-rich inclusions from unequilibrated ordinary chondrites. *Meteorit. Planet. Sci.* 54, S2, #6250.

Ebert S., Nagashima K., Krot A. N. and Bischoff A. (2020) Oxygen-isotope heterogeneity in the Northwest Africa 3358 (H31.) refractory inclusions – fluid-assisted isotopic exchange on the H-chondritic parent body. *Geochim. Cosmochim. Acta* 282, 98-112.

Fisher G. W. and Medaris L. G., Jr. (1969) Cell dimensions and X-ray determinative curve for synthetic Mg-Fe olivines. *Am. Miner.* 54, 741-753.

Fluegel A. (2007) Global model for calculating room-temperature glass density from the composition. *J. Am. Ceram. Soc.* 90, 2622-2625.

Gerber S., Burkhardt C., Budde G., Metzler K. and Kleine T. (2017) Mixing and transport of dust in the early solar nebula as inferred from titanium isotope variations among chondrules. *Astrophys. J.Astrophys. J. Lett.* 841, L17.

Greenwood R. C. and Franchi I. A. (2004) Alteration and metamorphism of CO3 chondrites: Evidence from oxygen and carbon isotopes. *Meteorit. Planet. Sci.* 39, 1823−1838.

Grossman J. N. and Brearley A. J. (2005) The onset of metamorphism in ordinary and carbonaceous chondrites. *Meteorit. Planet. Sci.* 40, 87-122.

Grossman L., Ganapathy R., Methot R. L. and Davis A. M. (1979) Trace elements in the Allende meteorite-IV. Amoeboid olivine aggregates. *Geochim. Cosmochim. Acta* 43, 817−829.

Grossman J. N., Rubin A. E. and MacPherson G. J. (1988) ALH 85085: A unique volatile-poor carbonaceous chondrite with possible implications for nebular fractionation processes. *Earth Planet Sci. Lett.* 91, 33–54.

Grossman J. N., Alexander C. M. O'D., Wang J. and Brearley A. J. (2000) Bleached chondrules: Evidence for widespread aqueous processes on the parent asteroids of ordinary chondrites. *Meteorit. Planet. Sci. 35, 467-486.*

Grossman J. N., Alexander C. M. O'D., Wang J. and Brearley A. J. (2002) Zoned chondrules in Semarkona: Evidence for high- and low-temperature processing. *Meteorit. Planet. Sci. 37, 49-73.*

Guan Y., Huss G. R., Leshin L. A., MacPherson G. J. and McKeegan K. D. (2006) Oxygen isotope and ^{26}Al-^{26}Mg systematics of aluminum-rich chondrules from unequilibrated enstatite chondrites. *Meteorit. Planet. Sci.* 41, 33−47.

Haugbølle T., Weber P., Wielandt D. P., Benítez-Llambay P., Bizzarro M., Gressel O. and Pessah M. E. (2019) Probing the Protosolar disk using dust filtering at gaps in the Early Solar System. *Astrophys. J.* 158, 55.

Herbst W. and Greenwood J. P. (2016) A new mechanism for chondrule formation: Radiative heating by hot planetesimals. *Icarus* 267, 364-367.

Huss G. R., MacPherson G. J., Wasserburg G. J., Russell S. S. and Srinivasan G. (2001) Aluminum-26 in calcium-aluminum-rich inclusions and chondrules from unequilibrated ordinary chondrites. *Meteorit. Planet. Sci.* 36, 975-997.

Ireland T. R., Fahey A. J. and Zinner E. K. (1991) Hibonite-bearing microspherules: A new type of refractory inclusions with large isotopic anomalies. *Geochim. Cosmochim. Acta* 55, 367–379.

Itoh S., Kojima H. and Yurimoto H. (2004) Petrography and oxygen isotopic compositions in refractory inclusions from CO chondrites. *Geochim. Cosmochim. Acta* 68, 183−194.

Itoh S., Russell S. S. and Yurimoto H. (2007) Oxygen and magnesium isotopic compositions of amoeboid olivine aggregates from the Semarkona LL3.0 chondrite. *Meteorit. Planet. Sci.* 42, 1241−1247.

Jacquet E., Piani L. and Weisberg M. K. (2018) Chondrules in Enstatite Chondrites. In *Chondrules*, edited by Russell S. S., Connolly Jr. H. C., and Krot A. N., Cambridge, University Press, pp. 175-195.

Jacquet E., Pignatale F. C., Chaussidon M. and Charnoz S. (2019) Fingerprints of the protosolar cloud collapse in the Solar System. II. Nucleosynthetic anomalies in meteorites. *Astrophys. J.* 884, 32.

Jones R. H., Villeneuve J. and Libourel G. (2018) Thermal histories of chondrules: Petrologic observations and experimental constrains. In *Chondrules*, edited by Russell S. S., Connolly Jr. H. C., and Krot A. N., Cambridge, University Press, pp. 57-90.

Kerraouch I., Ebert S., Patzek M., Bischoff A., Zolensky M. E., Pack A., Schmitt-Kopplin P., Belhai D., Bendaoud A. and Le L. (2019). A light, chondritic xenolith in the Murchison (CM) chondrite – Formation by fluid-assisted percolation during metasomatism? *Geochemistry* 79, #125518.

Kita T. N., Ushikubo T., Fu B. and Valley J. W. (2009) High precision SIMS oxygen isotope analysis and the effect of sample topography. *Chemical Geology* 264, 43−57.

Kita T. N., Nagahara H., Tachibana S., Tomomura S., Spicuzza M. J., Fournelle J. H. and Valley J. W. (2010) High precison SIMS oxygen three isotope study of chondrules in LL3 chondrites: Role of ambient gas during chondrules formation. *Geochim. Cosmochim. Acta* 74, 6610−6635.

Kööp L., Nakashima D., Heck P. R., Kita N. T., Tenner T. J., Krot A. N., Nagashima K., Park C. and Davis A. M. (2016) New constraints for the relationship between ^{26}Al and oxygen, calcium, and titanium isotopic variation in the early Solar System from a multi-element isotopic study of Spinel-Hibonite Inclusions. *Geochim. Cosmochim. Acta* , 184, 151–172.

Krot A. N. (2019) Refractory inclusions in carbonaceous chondrites: Records of early solar system processes. *Meteorit. Planet. Sci.* 54, 1647−1691.

Krot A. N. and Rubin A. E. (1994). Glass-rich chondrules in ordinary chondrites. *Meteorit. Planet. Sci.* 29, 697−707.

Krot A. N. and Keil K. (2002) Anorthite-rich chondrules in CR and CH carbonaceous chondrites: Genetic link between Ca-Al-rich inclusions and ferromagnesian chondrules. *Meteorit. Planet. Sci.* 37, 99−111.

Krot A. N., Hutcheon I. D. and Keil. K. (2002) Plagioclase-rich chondrules in the reduced CV chondrites: Evidence for complex formation history and genetic links between calcium-aluminum-rich inclusions and ferromagnesian chondrules. *Meteorit. Planet. Sci.* 37, 155−182.

Krot A. N., Fagan T. J., Keil K., McKeegan K. D., Sahijpal S., Hutcheon I. D., Petaev M. I. and Yurimoto H. (2004) Ca,Al−rich inclusions, amoeboid olivine aggregates, and Al-rich chondrules from the unique carbonaceous chondrite Acfer 094: I. Mineralogy and petrology. *Geochim. Cosmochim. Acta* 68, 2167−2184.

Krot A. N., McKeegan K. D., Huss G. R., Liffman K., Sahijpal S., Hutcheon I. D., Srinivasan G., Bischoff A. and Keil K. 2006a. Aluminum-Magnesium and oxygen isotope study of relict Ca-Al-rich inclusions in chondrules. *Astrophys. J.* 639, 1227−1237.

Krot A. N., Yurimoto H., McKeegan K. D., Leshin L., Chaussidon M., Libourel G., Yoshitake M., Huss G. R., Guan Y. and Zanda B. (2006b) Oxygen isotopic compositions of chondrules: Implications for evolution of oxygen isotopic reservoirs in the solar nebula. *Chemie Erde* 66, 249−276.

Krot A. N., Amelin Y., Bland P., Ciesla F. J., Connelly J., Davis A. M., Huss G. R., Hutcheon I. D., Makide K., Nagashima K., Nyquist L. E., Russell S. S., Scott E. R. D., Thrane K., Yurimoto H. and Yin Q.-Z. (2009) Origin and chronology of chondritic components: A review. *Geochim. Cosmochim. Acta* 73, 4963−4997.

Krot A. N., Nagashima K., E. M. M. van Kooten and Bizzarro M. (2017a) Calcium-aluminum-rich inclusions recycled during formation of porphyritic chondrules from CH carbonaceous chondrites. *Geochim. Cosmochim. Acta* , 201, 185–223.

Krot A. N., Nagashima K., van Kooten E. M. M. and Bizarro M (2017b) High-temperature rims around calcium-aluminum-rich inclusions from the CR, CB and CH carbonaceous chondrites. *Geochim. Cosmochim. Acta* 201, 155−184.

Krot A. N., Nagashima K., Libourel G. and Miller K. E. (2018) Multiple mechanism of transient heating events in the protoplanetary disk: Evidence from precursors of chondrules and igneous Ca,Al-rich inclusions. In *Chondrules*, edited by Russell S. S., Connolly Jr. H. C., and Krot A. N., Cambridge, University Press, pp. 11-56.Krot A. N., Nagashima K., Simon S. B., Ma C. and Connolly H. C. (2019a) Mineralogy, petrography, and oxygen and aluminum-magnesium isotope systematics of grossite-bearing refractory inclusions. *Geochemistry* 79, 125529.

Krot A. N., Nagashima K., Fintor K. and Pa´l-Molna´r E. (2019b) Evidence for oxygen-isotope exchange in refractory inclusions from Kaba (CV3.1) carbonaceous chondrite during fluid-rock interaction on the CV parent asteroid. *Geochim. Cosmochim. Acta* 246, 419–435

Kruijer T. S., Burkhardt C., Budde G. and Kleine T. (2017) Age of Jupiter inferred from the distinct genetics and formation times of meteorites. *Proc. Natl. Acad. Sci.* 114, 6712−6716.

Kruijer T. S., Kleine T. and Borg L. E. (2020) The great isotopic dichotomy of the early Solar System. *Nature Astronomy* 4, 32−40.

Leya I., Schönbächler M. Krähenbühl, U. and Halliday A. N. (2009) New titanium isotope data for Allende and Efremovka CAIs. *Astrophys. J.* 702, 1118−1126.

Liffman K., Cuello N. and Paterson D. A. (2016) A unified framework for producing CAI melting, Wark–Lovering rims and bowl-shaped CAIs. *Mon. Not. R. Astron. Soc. Lett.* 462, 1137−1163.

Lodders K., Palme H. and Gail H. P. (2009) Abundances of the elements in the solar system. In Landolt-Börnstein, New Series, Vol. VI/4B, Chap. 4.4 (ed. J. E. Trümper). Springer-Verlag, Berlin, Heidelberg, New York, pp. 560–630.

MacPherson G. J. (2014) Calcium–aluminum-rich inclusions in chondritic meteorites, in: A.M. Davis (Ed.) H.D. Holland, K.K. Turekian (Eds.), *Meteorites and Cosmochemical Processes*, Treatise on Geochemistry, Vol. 1, Elsevier, Oxford (2014), pp. 139–179.

MacPherson G. J. and Huss G. R. (2005) Petrogenesis of Al-rich chondrules: Evidence from bulk compositions and phase equilibria. *Geochim. Cosmochim. Acta* 69, 3099−3127.

MacPherson G. J., Wark D. A. and Armstrong J. T. (1988) Primitive material surviving in chondrites: refractory inclusions. In *Meteorites and the Early Solar System* (eds. J. F. Kerridge and M. S. Matthews). Univ. Arizona Press, Tucson, pp. 746–807.

MacPherson G. J., Huss G. R. and Davis A. M. (2003) Extinct ^{10}Be in Type A calcium-aluminum-rich inclusions from CV chondrites. *Geochim. Cosmochim. Acta* 67, 3165–3179.

Makide K., Nagashima K., Krot A. N., Huss G. R., Hutcheon I. D. and Bischoff A. (2009) Oxygen- and magnesium-isotope compositions of calcium-aluminum-rich inclusions from CR2 carbonaceous chondrites. *Geochim. Cosmochim. Acta* 73, 5018−5050.

Marrocchi Y., Villeneuve J., Batanova V., Piani L. and Jacquet E. (2018). Oxygen isotopic diversity of chondrule precursors and the nebular origin of chondrules. *Earth Planet Sci. Lett.Earth Planet Sci. Lett.* 496, 132−141.

Marrocchi Y., Euverte R., Villeneuve J., Batanova V., Welsch B., Ferrière L. and Jacquet E. (2019) Formation of CV chondrules by recycling of amoeboid olivine aggregate-like precursors. *Geochim. Cosmochim. Acta* 247, 121−141.

Mason B. and Martin P. M. (1977) Geochemical differences among components of the Allende meteorite. *Smithsonian Contribution to the Earth Sciences* 19, 84−95.

Mathieu R., Libourel, G., Deloule E., Tissandier L., Rapin C. and Podor R. (2011) Na_2O solubility in CaO-MgO-SiO_2 melts. *Geochim. Cosmochim. Acta* 75, 608-628.

McKeegan K. D., Leshin L. A., Russell S. S. and MacPherson G. J. (1998) Oxygen isotopic abundances in calcium-aluminum-rich inclusion from ordinary chondrites: Implications for nebular heterogeneity. *Science* 280, 414−418.

McKeegan K. D., Chaussidon M. and Robert F. (2000) Incorporation of short-lived ^{10}Be in a calcium-aluminum–rich inclusion from the Allende meteorite. *Science* 289, 1334–1337.

McKeegan K. D., Kallio A. P., Heber V. S., Jarzebinski G., Mao P. H., Coath C. D., Kunihiro T., Wiens R. C., Nordholt J. E., Moses R. W. Jr., Reisenfeld D. B., Jurewicz J. G. and Burnett D.S. (2011) The oxygen isotopic composition of the Sun inferred from captured solar wind. *Science* 332, 1528−1532.

Metzler K. and Pack A. (2016) Chemistry and oxygen isotopic composition of cluster chondrite clasts and their components in LL3 chondrites. *Meteorit. Planet. Sci.* 51, 276−302.

Morris M. A., Boley A. C., Desch S. J. and Athanassiadou T. (2012) Chondrule formation in bow shocks around eccentric planetary embryos. *Astrophys. J.Astrophys. J. Lett.* 752, L27.

Nagahara H. and Kushiro I. (1982) Calcium-aluminium-rich chondrules in the unequilibrated ordinary chondrites. *Meteoritics* 17, 55−63.

Nagahara H., Kita N. T., Ozawa K. and Morishita Y. (2008) Condensation of major elements during chondrule formation and its implication to the origin of chondrules. *Geochim. Cosmochim. Acta* 72, 1442–1465.

Nagashima K., Krot A. N. and Huss G. R. (2015) Oxygen-isotope composition of chondrules phenocryst and matrix grains in Kakangari K-grouplet chondrite: Implications to a chondrule-matrix genetic relationship. *Geochim. Cosmochim. Acta* 151, 49−67.

Nagashima K., Libourel G., Portail M. and Krot A. N. (2020) Magnesium-isotope compositions in a compound amoeboid olivine aggregate-chondrule object from Acfer 094 meteorite. *Lunar Planet. Sci.* **51**, #2576.

Nanne J. A. M., Nimmo F., Cuzzi J. N. and Kleine Thorsten (2019) Origin of the non-carbonaceous–carbonaceous meteorite dichotomy. *Earth Planet Sci. Lett.* 511, 44−54.

Niederer F. R., Papanastassiou D. A. and Wasserburg G. J. (1981) The isotopic composition of titanium in the Allende and Leoville meteorites. *Geochim. Cosmochim. Acta* 45, 1017−1031.

Niemeyer S. (1988a) Titanium isotopic anomalies in chondrules from carbonaceous chondrites. *Geochim. Cosmochim. Acta* 52, 309−318.

Niemeyer S. (1988b) Isotopic diversity in nebular dust: The distribution of Ti isotopic anomalies in carbonaceous chondrites. *Geochim. Cosmochim. Acta* 52, 2941−2954.

Niemeyer S. and Lugmair G. W. (1981) Ubiquitous isotopic anomalies in Ti from normal Allende inclusions. *Earth Planet Sci. Lett.* 53, 211−225.

Pape J., Mezger K., Bouvier A.-S. and Baumgartner L. P. (2019) Time and duration of chondrule formation: Constraints from ^{26}Al-^{26}Mg ages of individual chondrules. *Geochim. Cosmochim. Acta* 244, 416-436.

Piralla M., Villeneuve J., Batanova V., Jacquet E. and Marrocchi Y. (2021) Conditions of chondrule formation in ordinary chondrites. Geochim. Cosmochim. Acta 313, 295–312.

Render J., Ebert S., Burkhardt C., Kleine T. and Brennecka G. A. (2019) Titanium isotopic evidence for a shared genetic heritage of refractory inclusions from different carbonaceous chondrites. *Geochim. Cosmochim. Acta* 254, 40−53.

Rout S.S. and Bischoff A. (2008) Ca,Al-rich inclusions in Rumuruti (R) chondrites. *Meteorit. Planet. Sci.* 43, 1439−1464.

Rudraswami N. G., Ushikubo T., Nakashima D. and Kita N. T. (2011) Oxygen isotope systematics of chondrules in the Allende CV3 chondrite: High precision ion microprobe studies. *Geochim. Cosmochim. Acta* 75, 7596–7611.

Russell S. S., Huss G. R., Fahey A. J., Greenwood R. C., Hutchison R. and Wasserburg G. J. (1998) An isotopic and petrologic study of calcium-aluminum-rich inclusions from CO3 meteorites. *Geochim. Cosmochim. Acta* 62, 689–714.Russell S. S., MacPherson G. J., Leshin L. A. and McKeegan K. D., (2000) ^{16}O enrichments in aluminum-rich chondrules from ordinary chondrites, *Earth Planet Sci. Lett.s* 184, 57-74.

*Meteorit. Planet. Sci.*Russell S. S., Itoh S., Salge T., Higashi Y., Kawasaki N. and Sakamoto N. (2016) A CAI in the highly unequilibrated ordinary chondrite Northwest Africa 8276: Implications for CAI formation and processing. *Lunar Planet. Sci.* 47, #1989.

Ryerson F. J. and McKeegan D. (1994) Determination of oxygen self-diffusion in åkermanite, anorthite, diopside, and spinel: Implications for oxygen isotopic anomalies and the thermal histories of Ca-Al-rich inclusions. *Geochim. Cosmochim. Acta* 58, 3713−3734.

Shollenberger Q. R., Borg L. E., Render J., Ebert S., Bischoff A., Russell S. S. and Brennecka G. A. (2018) Isotopic coherence of refractory inclusions from CV and CK meteorites: Evidence from multiple isotopic systems. *Geochim. Cosmochim. Acta* 228, 62−80.

Shu F. H., Shang H. and Lee T. (1996) Toward an astrophysical theory of chondrites. *Science* 271, 1545−1552.

Simon S. B., Davis A. M., Grossman L. and Zinner E. K. (1998) Origin of hibonite-pyroxene spherules found in carbonaceous chondrites. *Meteorit. Planet. Sci.* 33, 411-424.

Tenner T. J., Ushikubo T., Kurahashi E., Kita N. T. and Nagahara H. (2013) Oxygen isotope systematics of chondrule phenocryst from the CO3.0 chondrite Yamato 81020: Evidence for two distinct oxygen isotope reservoirs. *Geochim. Cosmochim. Acta* 103, 226−245.

Tomeoka K. and Itoh D. (2004) Sodium-metasomatism in chondrules in CO3 chondrites: Relationship to parent body thermal metamorphism. *Meteorit. Planet. Sci.Meteorit. Planet. Sci.* 39, 1359-1373.

Trinquier A., Elliott T., Ulfbeck D., Coath C., Krot A. N. and Bizzarro M. (2009) Origin of nucleosynthetic isotope heterogeneity in the solar protoplanetary disk. *Science* 324, 374−376.

Tronche E. J., Hewins R. H. and MacPherson G. J. (2007) Formation conditions of aluminum-rich chondrules. *Geochim. Cosmochim. Acta* 148, 228-250.

Ushikubo T., Kimura M., Kita N. T. and Valley J. W. (2012) Primordial oxygen isotope reservoirs of the solar nebula recorded in chondrules in Acfer 094 carbonaceous chondrite. *Geochim. Cosmochim. Acta* 90, 242−264.

Ushikubo T., Tenner T. J., Hicagon H. and Kita N. T. (2017) A long duration of the ^{16}O-rich reservoir in the solar nebula, as recorded in fine-grained refractory inclusions from the least metamorphosed carbonaceous chondrites. *Geochim. Cosmochim. Acta* 201, 103−122.

Van Kooten E. M. M. E., Wielandt D., Schiller M., Nagashima K., Thomen A., Larsen K. K., Olsen M. B., Nordlund Å., Krot A. N. and Bizzarro M. (2016) Isotopic evidence for primordial molecular cloud material in metal-rich carbonaceous chondrites. *Proc. Natl. Acad. Sci.* 113, 2011−2016.

Warren P. H. (2011) Stable-isotopic anomalies and the accretionary assemblage of the Earth and Mars: a subordinate role for carbonaceous chondrites. *Earth Planet Sci. Lett.* 311, 93−100.

Wasson J. T., Yurimoto H. and Russell S. S. (2001) ^{16}O-rich melilite in CO3.0 chondrites: Possible formation of common, ^{16}O poor melilite by aqueous alteration. *Geochim. Cosmochim. Acta* 65, 4539−4549.

Weber P., Benítez-Llambay P., Gressel O., Krapp L. and Pessah M. E. (2018) Characterizing the variable dust permeability of planet-induced gaps. *Astrophys. J.* 854, 153.

Wielandt D., Nagashima K., Krot A. N., Huss G. R., Ivanova M. A. and Bizzarro M. (2012) Evidence for multiple sources of 10Be in the early solar system. *Astrophys. J.* 74, L25–L28.

Williams C. D., Janney P. E., Hines R. R. and Wadhwa M. (2016) Precise titanium isotope compositions of refractory inclusions in the Allende CV3 chondrite by LA-MC-ICPMS. *Chemical Geology* 436, 1−10.

Wood B. J., Smythe D. J. and Harrison T. (2019) The condensation temperatures of the elements: A reappraisal. *American Mineralogist* 104, 844-856.

Yang L. and Ciesla F. J. (2012) The effects of disk building on the distribution of refractory materials in the solar nebula. *Meteorit. Planet. Sci.* 47, 99−119.

Young E. D. and Russell S. S. (1998) Oxygen reservoirs in the early solar nebula inferred from an Allende CAI. *Science* 282, 452−455.

Zhang A. and Hsu W. (2009) Refractory inclusions and aluminum-rich chondrules in Sayh al Uhaymir 290 CH chondrite: Petrography and mineralogy. *Meteorit. Planet. Sci.* 44, 787−804.

Zhang A.-C., Itoh S., Sakamoto N., Wang R.-C. and Yurimoto H. (2014) Origins of Al-rich chondrules: Clues from a compound Al-rich chondrule in the Dar al Gani 978 carbonaceous chondrite. *Geochim. Cosmochim. Acta* 130, 78−92.

Zhang M., Lin Y., Tang G., Liu Y. and Leya I. (2020) Origin of Al-rich chondrules in CV chondrites: Incorporation of diverse refractory components into the ferromagnesian chondrule-forming region. *Geochim. Cosmochim. Acta* 272, 198−217.

Tables:

Table 1: Basic characteristics of 21 studied (Na-)Al-rich chondrules.

Object	Meteorite	Type	size [µm]	mineralogy
NaC-1	NWA 3358	H3.10	150	gl, px
NaC-2	NWA 3358	H3.10	330x300	gl, ol, px
NaC-3	NWA 3358	H3.10	160	gl, ol
NaC-4	NWA 3358	H3.10	340	gl, qz
NaC-5	NWA 3358	H3.10	340	gl, px, ol
NaC-6	NWA 3358	H3.10	250	gl, ol, px
NaC-7	Adrar 003	L/LL3.10	300x250	gl, ol, px
NaC-8	Adrar 003	L/LL3.10	950x850	gl, ol, px
NaC-9	Adrar 003	L/LL3.10	470x430	gl, ol, px
NaC-10	Krymka	LL3.20	500x370	gl, px
NaC-11	Krymka	LL3.20	330x250	gl, ol
NaC-12	Krymka	LL3.20	400	gl, ol
NaC-13	NWA 8580	L3.15	750x450	gl, px, ol
NaC-14	NWA 8580	L3.15	450x350	gl, ol
Ca-Al-1	NWA 3358	H3.10	550	px, gl, sp
Ca-Al-2	NWA 8580	L3.15	550 (fr)	gl, px, sp, hib
Ca-Al-3	Vicencia	LL3.20	850x700	px, gl, ol
CO-NaC-1	DaG 083	CO3	540x500	gl, px, ol
CO-NaC-2	DaG 083	CO3	200x170	px, gl
CO-Ca-Al-1	DaG 083	CO3	1150	gl, ol, sp, px
CO-Ca-Al-2	DaG 083	CO3	210x190	px, ol, sp

Table 2: Compositions of mineral phases observed as porphyritic grains within the (Na)-Al-rich chondrules as obtained by electron microprobe analysis. Al-3 was added to study in at a later time and no microprobe data are available; data in wt%. --- = not detected

Olivine	MgO	Al_2O_3	SiO_2	CaO	FeO	TiO_2	Cr_2O_3	MnO	Total	Fo
NaC-2	55.7	0.07	41.7	0.19	1.06	nd	0.15	---	98.9	0.99
NaC-3	56.0	0.08	41.5	0.25	1.48	nd	0.16	0.08	99.5	0.99
NaC-5	56.1	0.16	41.5	0.20	1.25	0.16	0.21	---	99.7	0.99
NaC-6	56.6	0.10	41.7	0.34	0.36	nd	0.17	---	99.2	1.00
NaC-7	56.6	0.15	41.1	0.28	0.86	nd	0.28	0.12	99.5	0.99
NaC-8	56.6	0.14	41.6	0.37	0.58	nd	0.21	---	99.6	0.99
NaC-9	57.0	0.05	41.5	0.23	0.51	0.11	0.12	0.07	99.6	1.00
NaC-11	56.1	0.14	42.2	0.27	0.45	nd	0.17	0.07	99.5	1.00
NaC-12	56.3	0.04	42.0	0.26	1.12	nd	0.14	0.07	100.0	0.99
NaC-13	56.1	0.09	41.5	0.27	1.43	0.10	0.15	---	99.7	0.99
NaC-14-1	55.8	0.09	40.7	0.26	2.50	nd	0.11	0.22	99.7	0.98
NaC-14-2*	56.8	0.18	41.3	0.43	0.73	nd	0.19	---	99.7	0.99
CO-NaC-1	56.6	0.03	42.0	0.28	0.93	nd	0.16	---	100.1	0.99
CO-Al-1	56.9	0.21	41.7	0.61	0.52	nd	0.08	---	100.1	0.99
CO-Al-2	56.8	0.15	41.7	0.57	1.18	nd	0.23	---	100.7	0.99

Ca pyroxene	MgO	Al_2O_3	SiO_2	CaO	FeO	TiO_2	Cr_2O_3	MnO	Total	Wo	Fs
NaC-1	18.6	6.9	50.2	19.9	0.43	2.27	0.30	0.10	98.7	0.43	0.01
NaC-2	16.5	9.5	48.4	21.3	0.43	1.93	0.82	0.15	99.1	0.48	0.01
NaC-5	22.2	7.3	50.0	16.2	0.37	1.60	0.32	0.06	98.1	0.34	0.01
NaC-6	16.8	9.6	49.0	21.3	0.37	1.68	0.38	0.13	99.2	0.47	0.01
NaC-7	19.7	8.5	49.5	17.3	0.87	1.79	0.99	0.23	98.9	0.38	0.01
NaC-8	20.3	5.7	51.4	18.3	0.95	1.29	1.12	0.19	99.3	0.39	0.02
NaC-9	16.3	12.7	47.3	20.1	0.30	1.72	0.78	0.13	99.4	0.47	0.01
NaC-10	18.3	7.7	50.3	19.9	0.70	1.54	1.15	0.17	99.7	0.43	0.01
NaC-13	18.2	10.9	49.1	19.5	0.19	1.50	0.26	---	99.7	0.43	0.00
Al-1	21.0	10.3	49.3	17.4	0.13	1.18	0.18	---	99.5	0.37	0.00
Al-2	7.7	24.4	37.3	24.8	0.15	4.3	0.33	---	98.9		
CO-NaC-1	18.1	7.7	50.5	20.8	0.43	1.95	0.60	---	100.1	0.45	0.01

CO-Al-1	17.8	15.16	46.4	16.83	0.41	1.64	1.34	0.35	99.9	0.40	0.01
CO-Al-2	13.5	14.3	45.5	24.4	0.24	1.7	0.4	---	100.1	0.56	0.00

Low-Ca pyroxene	MgO	Al_2O_3	SiO_2	CaO	FeO	TiO_2	Cr_2O_3	MnO	Total	Wo	Fs
NaC-1	35.9	2.45	56.5	2.51	0.39	0.70	0.32	---	98.9	0.05	0.01
NaC-2	35.8	2.21	56.8	2.63	0.77	0.41	0.54	0.12	99.3	0.05	0.01
NaC-5	28.4	8.7	51.1	8.5	0.48	1.28	0.39	0.06	98.9	0.18	0.01
NaC-7	34.8	2.32	55.9	4.4	1.11	0.36	0.70	0.24	99.9	0.08	0.02
NaC-8	35.4	2.95	56.1	2.23	1.05	0.43	1.04	0.16	99.4	0.04	0.02
NaC-9	36.7	1.97	57.5	2.65	0.79	0.64	0.56	0.14	100.9	0.05	0.01
NaC-10	38.0	1.67	58.0	0.50	0.72	0.42	0.58	---	100.0	0.01	0.01
Al-1	33.8	5.7	54.5	3.9	0.16	0.82	0.16	---	99.2	0.08	0.00
CO-NaC-1	37.4	2.10	57.5	1.49	0.53	0.45	0.62	---	100.1	0.03	0.01

Spinel	MgO	Al_2O_3	SiO_2	CaO	FeO	TiO_2	Cr_2O_3	MnO	Total
Al-1	27.7	69.7	0.2	---	0.23	0.35	0.49	---	98.7
Al-2	27.5	70.1	nd	0.06	0.58	0.55	0.15	---	98.9
CO-Al-1	28.1	71.0	nd	---	0.37	0.28	0.17	---	100.0
CO-Al-2	27.5	69.0	0.1	0.10	1.00	nd	2.02	---	99.7

*Olivine measured by SIMS

--- = not detected or below detection limit

Table 3a: Oxygen isotopic composition of the ordinary chondrites' (Na-)Al-rich chondrules studied.

ordinary chondrites	Phase	$\delta^{18}O$ [‰]		2σ	$\delta^{17}O$ [‰]		2σ	$\Delta^{17}O$ [‰]		2σ
NaC-1	lpx-1	-0.93	±	1.40	-4.74	±	2.70	-4.26	±	2.79
	lpx-2	-0.31	±	1.26	-4.67	±	2.39	-4.51	±	2.48
	glass	8.24	±	1.18	9.27	±	2.03	4.99	±	2.12
NaC-2	ol	-1.47	±	1.78	-1.47	±	2.15	-0.71	±	2.34
	cpx	-2.42	±	1.46	-1.31	±	1.61	-0.05	±	1.78
	glass-1	5.48	±	1.46	7.09	±	2.14	4.24	±	2.27
	glass-2	5.46	±	1.27	6.16	±	1.81	3.32	±	1.93
NaC-3	ol	2.42	±	1.27	0.64	±	2.16	-0.62	±	2.26
	glass	8.45	±	1.17	7.67	±	1.88	3.28	±	1.98
NaC-4	glass-1	-10.81	±	1.39	-7.19	±	1.93	-1.57	±	2.06
	glass-2	-4.17	±	1.25	-1.54	±	2.00	0.62	±	2.11
NaC-5	ol	1.78	±	1.16	1.51	±	1.95	0.58	±	2.04
	lpx	1.71	±	1.22	2.27	±	2.00	1.39	±	2.10
	cpx	-0.21	±	1.37	0.66	±	1.41	0.77	±	1.58
	glass	4.75	±	1.32	6.52	±	1.97	4.05	±	2.09
NaC-6	ol	-1.19	±	1.36	-4.80	±	1.96	-4.19	±	2.08
	cpx	-6.46	±	1.51	-5.70	±	1.37	-2.34	±	1.58
	glass	8.77	±	1.21	5.75	±	1.96	1.19	±	2.06
Nac-7	sp	0.79	±	0.83	0.67	±	1.00	0.26	±	1.09
	ol	1.60	±	1.17	1.65	±	1.81	0.82	±	1.91
	glass	2.46	±	1.15	2.77	±	1.83	1.49	±	1.92
NaC-8	ol-1	3.46	±	1.12	0.53	±	2.04	-1.27	±	2.13
	ol-2	3.44	±	1.18	0.57	±	1.81	-1.21	±	1.91
	lpx	1.03	±	1.40	-0.38	±	1.75	-0.91	±	1.89
	glass	-1.24	±	1.37	0.61	±	2.06	1.26	±	2.18
NaC-9	ol	2.16	±	1.12	-1.53	±	1.75	-2.65	±	1.84
	glass	2.43	±	1.23	2.93	±	2.06	1.67	±	2.16
NaC-10	glass	13.15	±	1.26	9.33	±	2.18	2.49	±	2.28
NaC-11	ol	0.10	±	1.78	-2.28	±	3.09	-2.33	±	3.23
	glass	9.44	±	1.32	5.64	±	2.64	0.73	±	2.73
NaC-12	ol	5.29	±	1.27	3.91	±	2.26	1.15	±	2.35
	glass	2.03	±	1.63	0.71	±	2.11	-0.35	±	2.28
NaC-13	ol	-6.33	±	1.45	-7.75	±	2.05	-4.45	±	2.19
	cpx	-11.45	±	1.83	-8.19	±	1.75	-2.23	±	2.00
	glass	9.15	±	1.12	7.07	±	2.15	2.31	±	2.22

NaC-14	ol	1.70	±	1.30	1.49	±	2.00	0.60	±	2.11
	glass	6.02	±	1.33	5.39	±	2.01	2.26	±	2.13
Ca-Al-1	sp-1	-2.32	±	0.63	-3.58	±	1.38	-2.37	±	1.41
	sp-2	-1.77	±	0.64	-3.71	±	1.33	-2.79	±	1.37
	cpx	-4.86	±	1.37	-4.31	±	1.30	-1.78	±	1.48
	glass	4.95	±	1.23	8.41	±	2.15	5.84	±	2.24
Ca-Al-2	sp-1	-9.91	±	0.85	-7.45	±	1.23	-2.30	±	1.30
	hib-1	-9.43	±	0.80	-7.75	±	1.40	-2.84	±	1.46
	hib-2	-8.94	±	0.64	-8.25	±	1.28	-3.60	±	1.32
	cpx-1	-8.52	±	1.34	-6.71	±	1.33	-2.28	±	1.50
	cpx-2	-9.24	±	1.29	-6.24	±	1.55	-1.44	±	1.69
	glass	-6.38	±	1.28	-7.40	±	2.29	-4.08	±	2.39
Ca-Al-3	sp-1	-2.02	±	0.61	-3.45	±	1.20	-2.40	±	1.24
	sp-2	-2.90	±	0.78	-3.46	±	1.35	-1.95	±	1.41
	cpx-1	-7.51	±	1.51	-3.72	±	1.69	0.19	±	1.86
	cpx-2	-6.92	±	1.54	-4.63	±	2.02	-1.03	±	2.17
	gl	7.17	±	1.33	6.37	±	2.19	2.64	±	2.30

Table 3b: Oxygen isotopic composition of the CO3.1 chondrite's (Na-)Al-rich chondrules studied.

CO chondrites	Phase	$\delta^{18}O$ [‰]		2σ	$\delta^{17}O$ [‰]		2σ	$\Delta^{17}O$ [‰]		2σ
CO-NaC-1	lpx	-5.80	±	1.14	-10.42	±	1.76	-7.41	±	1.86
	ol	-3.18	±	1.10	-8.00	±	1.90	-6.34	±	1.99
	cpx	-7.37	±	1.37	-8.14	±	1.61	-4.31	±	1.76
	gl	-0.41	±	1.25	-1.99	±	2.00	-1.78	±	2.10
CO-NaC-2	cpx-1	-1.37	±	1.33	-3.49	±	1.73	-2.78	±	1.86
	cpx-2	-1.85	±	1.29	-4.55	±	1.30	-3.59	±	1.47
CO-Ca-Al-1	sp-1	-45.47	±	0.72	-48.25	±	1.19	-24.61	±	1.25
	sp-2	-45.50	±	0.65	-47.81	±	1.31	-24.15	±	1.36
	ol-1	-4.72	±	1.20	-8.72	±	1.74	-6.27	±	1.85
	ol-2	-4.48	±	1.14	-8.54	±	1.92	-6.21	±	2.01
	cpx	-7.60	±	1.34	-9.48	±	1.54	-5.52	±	1.69
	gl-1	-6.82	±	1.32	-8.49	±	1.96	-4.95	±	2.08
	gl-2	-7.42	±	1.22	-7.84	±	1.78	-3.98	±	1.89
CO-Ca-Al-2	sp	2.65	±	0.67	-0.83	±	1.53	-2.21	±	1.57
	ol	2.89	±	1.14	0.49	±	1.93	-1.02	±	2.02
	gl	3.47	±	1.37	1.53	±	2.03	-0.28	±	2.15

Table 4: Measured Na content from selected Al-rich glasses and olivine grains. Na bulk content and K_d rim/core are calculated as described in the text. The errors are based only on the uncertainty of the measured Na in rim and core.

Na_2O wt%	glass	bulk	ol rim	ol core	K_d rim	σ	K_d core	σ	K_d rim/core
NaC-2 - Line 1	13.0	5.7	0.0111	0.0050	0.0009	0.0002	0.0009	0.0004	0.9676
NaC-2 - Line 2	13.0	5.7	0.0143	0.0062	0.0011	0.0002	0.0011	0.0006	1.0053
NaC-2 - Line 3	13.0	5.7	0.0145	0.0060	0.0011	0.0002	0.0011	0.0005	1.0533
NaC-6 - Line 1	14.7	4.7	0.0219	0.0057	0.0015	0.0002	0.0012	0.0006	1.2401
NaC-6 - Line 2	14.7	4.7	0.0303	0.0068	0.0021	0.0002	0.0014	0.0006	1.4382
NaC-6 - Line 3	14.7	4.7	0.0196	0.0068	0.0013	0.0002	0.0014	0.0006	0.9303
NaC-13	13.0	5.4	0.0183	0.0054	0.0014	0.0002	0.0010	0.0006	1.4014
CO-NaC-1	14.0	4.1	0.0236	0.0035	0.0018	0.0002	0.0009	0.0007	1.9593
CO-Al-1 - Line 1	3.3	1.7	0.0052	0.0022	0.0016	0.0009	0.0013	0.0018	1.2342
CO-Al-1 - Line 2	3.3	1.7	0.0054	0.0018	0.0016	0.0009	0.0011	0.0018	1.5664

Figures:

FIGURE CAPTIONS:

Figure 1: Three Na-Al-rich chondrules from the H3.10 chondrite NWA 3358. On the left side are backscatter electron (BSE) images of the measured chondrules with marked O-isotope measurement spots and mineral phases. The right side shows the results of the O-isotope measurement within a three-isotope oxygen diagram in $\delta^{17}O$ *vs.* $\delta^{18}O$. $\Delta^{17}O = \delta^{17}O - (0.52 * \delta^{18}O)$. lpx = low-Ca pyroxene; cpx = Ca pyroxene; ol = olivine; gl = glass.

Figure 2: Three Na-Al-rich chondrules from the H3.10 chondrite NWA 3358. On the left side are backscatter electron (BSE) images of the measured chondrules with marked O-isotope measurement spots and mineral phases. The right side shows the results of O-isotope measurement within a three-isotope oxygen diagram in $\delta^{17}O$ *vs.* $\delta^{18}O$. $\Delta^{17}O = \delta^{17}O - (0.52 * \delta^{18}O)$. lpx = low-Ca pyroxene; cpx = Ca pyroxene; ol = olivine; gl = glass; qz = quartz.

Figure 3: Three Na-Al-rich chondrules from the L/LL3.10 chondrite Adrar 003. On the left side are backscatter electron (BSE) images of the measured chondrules with marked O-isotope measurement spots and mineral phases. The right side shows the results of the O-isotope measurement within a three-isotope oxygen diagram in $\delta^{17}O$ *vs.* $\delta^{18}O$. $\Delta^{17}O = \delta^{17}O - (0.52 * \delta^{18}O)$. lpx = low-Ca pyroxene; cpx = Ca pyroxene; ol = olivine; gl = glass; qz = quartz.

Figure 4: Three Na-Al-rich chondrules from the LL3.20 chondrite Krymka. On the left side are backscatter electron (BSE) images of the measured chondrules with marked O-isotope measurement spots and mineral phases. The right side shows the results of the O-isotope measurement within a three-isotope oxygen diagram in $\delta^{17}O$ *vs.* $\delta^{18}O$. $\Delta^{17}O = \delta^{17}O - (0.52 * \delta^{18}O)$. lpx = low-Ca pyroxene; cpx = Ca pyroxene; ol = olivine; gl = glass.

Figure 5: Two Na-Al-rich chondrules from the L3.15 chondrite NWA 8580. On the left side are backscatter electron (BSE) images of the measured chondrules with marked O-isotope measurement spots and mineral phases. The right side shows the results of the O-isotope measurement within a three-isotope oxygen diagram in $\delta^{17}O$ *vs.* $\delta^{18}O$. $\Delta^{17}O = \delta^{17}O - (0.52 * \delta^{18}O)$. cpx = Ca pyroxene; ol = olivine; gl = glass.

Figure 6: Three Al-rich chondrules from the H3.10 chondrite NWA 3358, the L3.15 chondrite NWA 8580, and the LL3.20 chondrite Krymka. On the left side are backscatter electron (BSE) images of the measured chondrules with marked O-isotope measurement spots and mineral phases. The right side shows the results of O-isotope measurement within a three-isotope oxygen diagram in $\delta^{17}O$ *vs.* $\delta^{18}O$. $\Delta^{17}O = \delta^{17}O - (0.52 * \delta^{18}O)$. hib = hibonite; sp= spinel; cpx = Ca pyroxene; ol = olivine; gl = glass.

Figure 7: Two Na-Al-rich chondrules from the CO chondrite Dar al Gani 083. On the left side are backscatter electron (BSE) images of the measured chondrules with marked O-isotope measurement spots and mineral phases. The right side shows the results of the O-isotope measurement within a three-isotope oxygen diagram in $\delta^{17}O$ *vs.* $\delta^{18}O$. $\Delta^{17}O = \delta^{17}O - (0.52 * \delta^{18}O)$. lpx = low-Ca pyroxene; cpx = Ca pyroxene; ol = olivine; gl = glass.

Figure 8: Two Al-rich chondrules from the CO chondrite Dar al Gani 083. On the left side are backscatter electron (BSE) images of the measured chondrules with marked O-isotope measurement spots and mineral phases. The right side shows the results of the O-isotope measurement within a three-isotope oxygen diagram in $\delta^{17}O$ *vs.* $\delta^{18}O$. $\Delta^{17}O = \delta^{17}O - (0.52 * \delta^{18}O)$. sp = spinel; cpx = Ca pyroxene; ol = olivine; gl = glass.

Figure 9: Various three-isotope oxygen diagrams of (Na-)Al-rich chondrules from ordinary chondrites. Small blue and red crosses are fayalite and magnetite formed by aqueous fluid on the parent body (Choi et al., 1998; Doyle et al., 2015; Ebert et al., 2020). TFL = terrestrial fraction line; Y&R = Young and Russel line (Young and Russell, 1998); PCM = primitive chondrule mineral line (Ushikubo et al., 2012); CCAM = carbonaceous chondrite anhydrous mineral line (Clayton et al., 1977).
a) All O-isotope measurements from constituents of (Na-)Al-rich chondrules from unequilibrated ordinary chondrites. b) Glass *vs.* phenocrysts: Glasses are colored-in circles and phenocrysts are in different shades of gray. c) Ca pyroxene (blue diamonds) *vs.* olivine (green triangles). Only Ca pyroxenes plot on the left side of the PCM or Y&R lines, indicating a shift to a more ^{18}O-enriched composition caused by matrix effects. d) Position of the Ca-Al-2 mineral phases compared to the mixing lines and the other chondrules (gray symbols). e) $\Delta^{17}O = \delta^{17}O - (0.52 * \delta^{18}O)$; dotted line: mean O-isotopic composition of

ordinary chondrites (Clayton et al., 1991); blueish line: O-isotopic composition of Fe,Mg chondrules from ordinary chondrite (Clayton et al. 1991, Metzler and Pack, 2016). hib = hibonite; sp = spinel; lpx = low-Ca pyroxene; ol = olivine; cpx = Ca pyroxene; gl = glass.

Figure 10: Three-isotope oxygen diagrams of constituents of (Na-)Al-rich chondrules from the CO3.1 chondrite Dar al Gani 083. TFL = terrestrial fraction line; Y&R = Young and Russel line (Young and Russell, 1998); PCM = primitive chondrule mineral line (Ushikubo et al., 2012); CCAM = carbonaceous chondrite anhydrous mineral line (Clayton et al., 1977). a) All O-isotope measurements from (Na-)Al-rich chondrules from DaG083. The relict spinel grains of CO-Ca-Al-1 plot in the area of CO CAIs. b) Close-up of the CO chondrite region. Small blue and red crosses are fayalite and magnetite formed by aqueous fluid on the parent body (Doyle et al., 2015). Small blue and green stars are bulk CO chondrites (Clayton and Mayeda, 1999; Greenwood and Franchi, 2004) and mean values of Fe,Mg chondrule phenocrysts from CO chondrites (Tenner et al., 2013)

Figure 11: The core and rim Na K_D values for various olivine grains from five different (Na)-Al-rich chondrules.

Figure 12: Various element measurements through two selected olivine grains, a) NaC-6 Line1 and b) NaC-2 Line3, creating a profile from one rim to another. White symbols are measurements that are not used for the K_D rim calculation. Because, in both cases, the rim measurements are influenced by the surrounding glass, which is visible by an increase of Fe and other elements. Furthermore, the cation number drops significantly away from what is typical and acceptable for olivine (calculated to 24 O anions, the cation number for olivine is 18).

Figure 13: a) Backscatter electron (BSE) image of the Na-Al-rich chondrule NaC-2 from the H3.1 chondrite NWA 3358. b) Ca map of NaC-2. The arrows mark the bright Ca rim around the chondrule. c) BSE image of the Al-rich chondrule Al-2 from the L3.15 chondrite NWA 8580. d) Ca map from Ca-Al-2. No clear Ca rim is visible even though the chondrule is in a chondrite of higher petrologic type than NaC-2.

Figures:

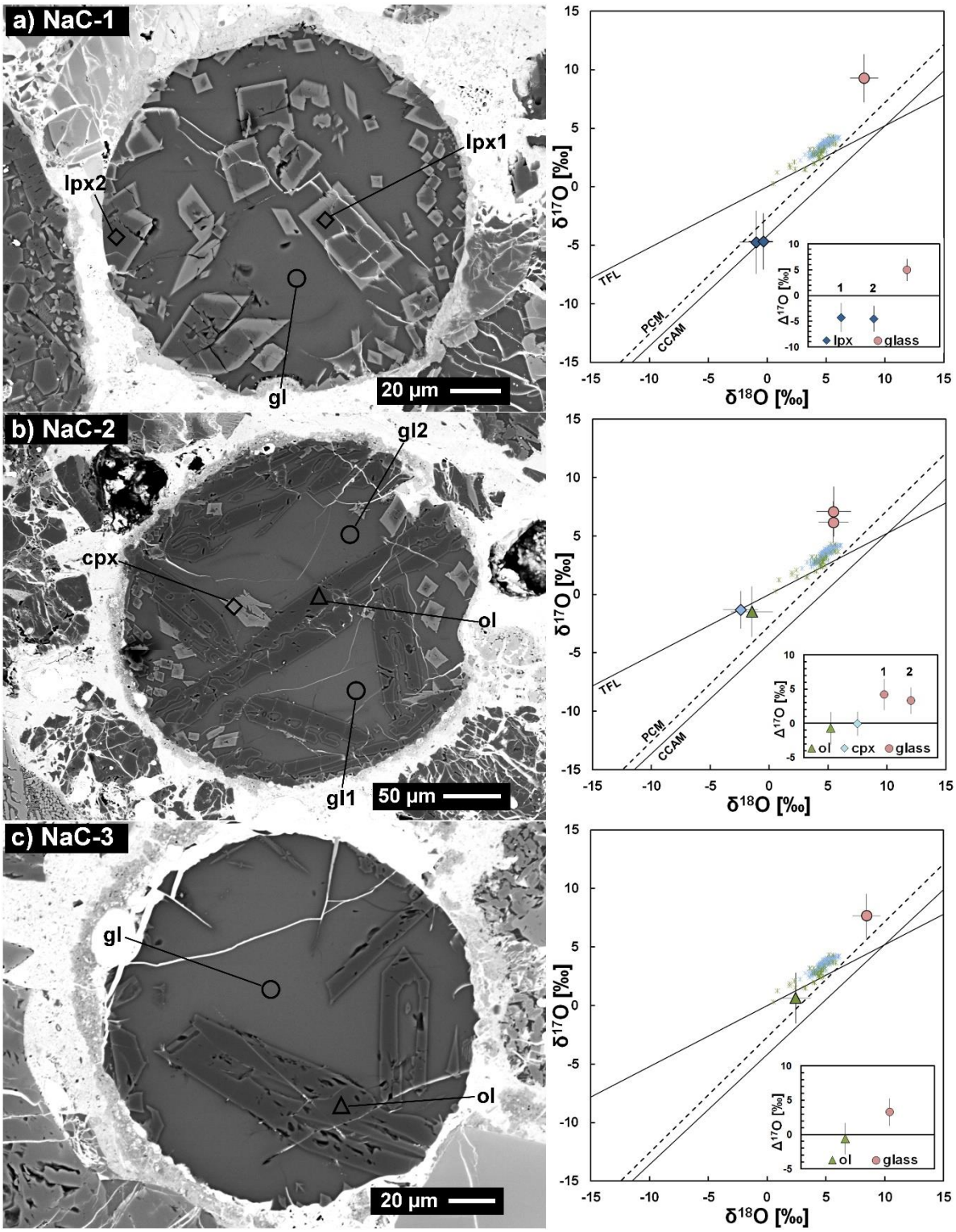

Figure 1:

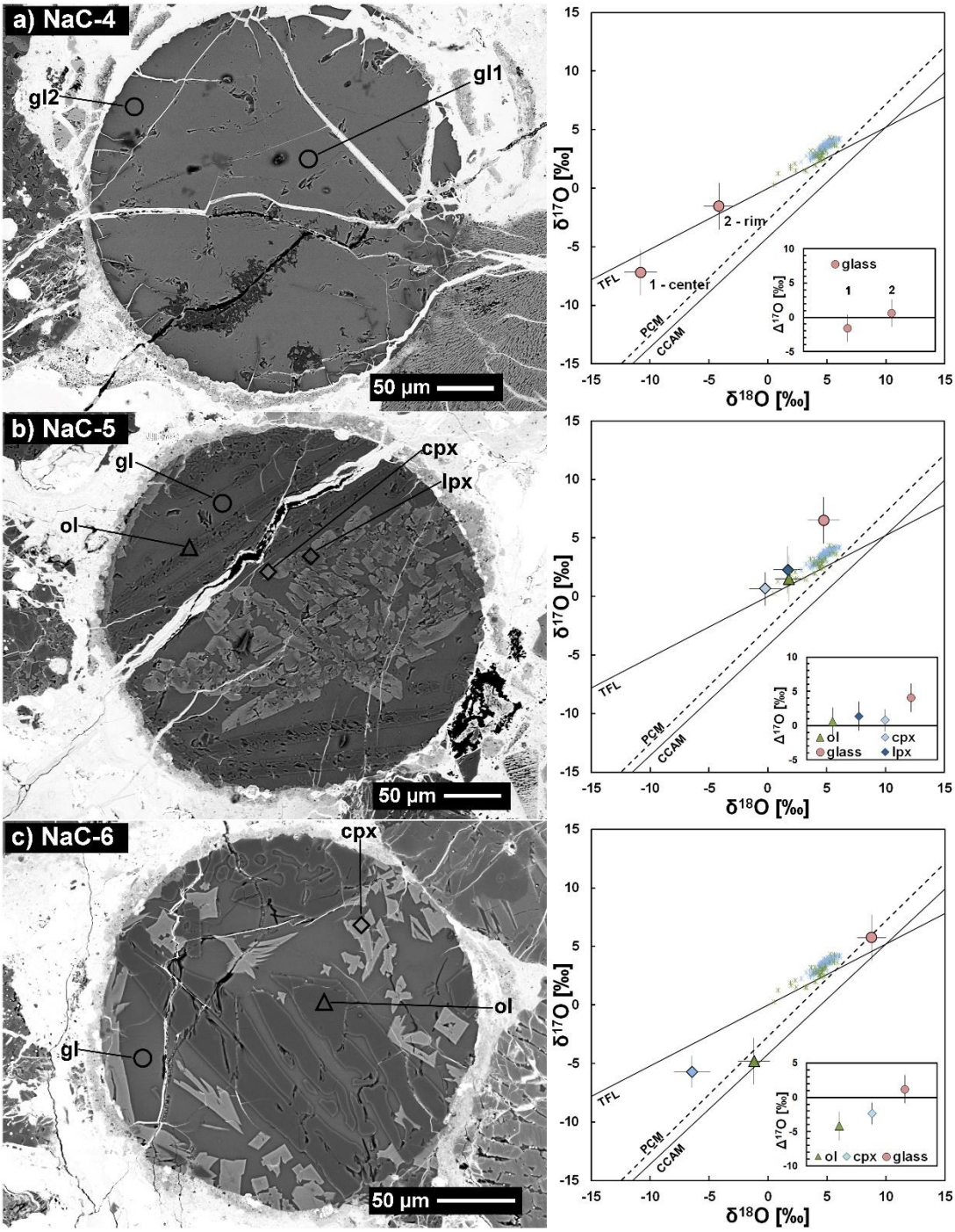
a) NaC-4
gl2
gl1
50 µm
2 - rim
1 - center
TFL
PCM
CCAM
glass
1
2
b) NaC-5
gl
cpx
lpx
ol
50 µm
ol
cpx
glass
lpx
c) NaC-6
cpx
ol
gl
50 µm
ol
cpx
glass
δ17O [‰]
δ18O [‰]
Δ17O [‰]

Figure 2:

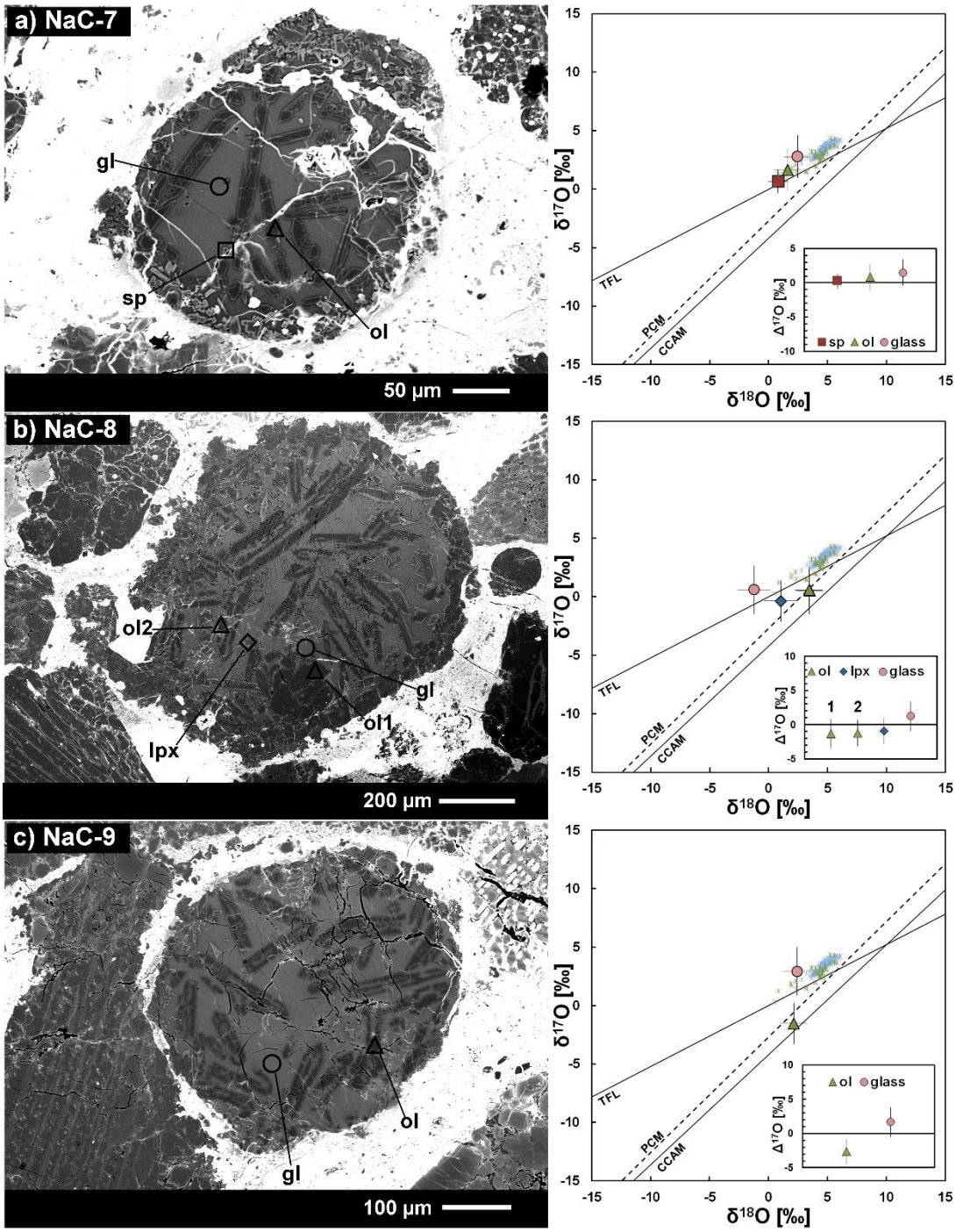
a) NaC-7
gl
sp
ol
50 µm
b) NaC-8
ol2
lpx
gl
ol1
200 µm
c) NaC-9
ol
gl
100 µm
δ17O [‰]
δ18O [‰]
TFL
PCM
CCAM
Δ17O [‰]
sp ol glass
ol lpx glass
1 2
ol glass

Figure 3:

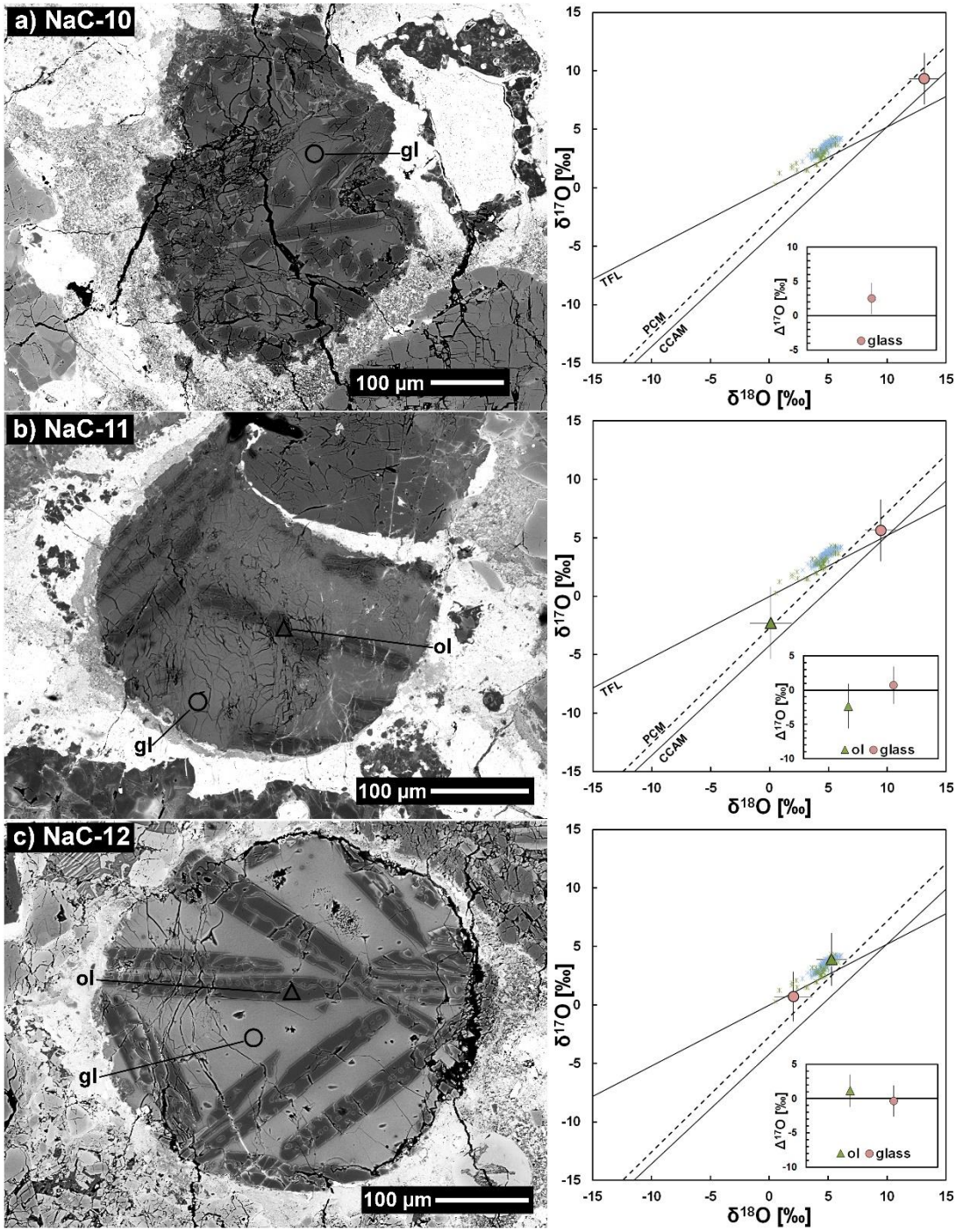
a) NaC-10
gl
100 µm
b) NaC-11
ol
gl
100 µm
c) NaC-12
ol
gl
100 µm
δ17O [‰]
δ18O [‰]
TFL
PCM
CCAM
Δ17O [‰]
glass
ol

Figure 4:

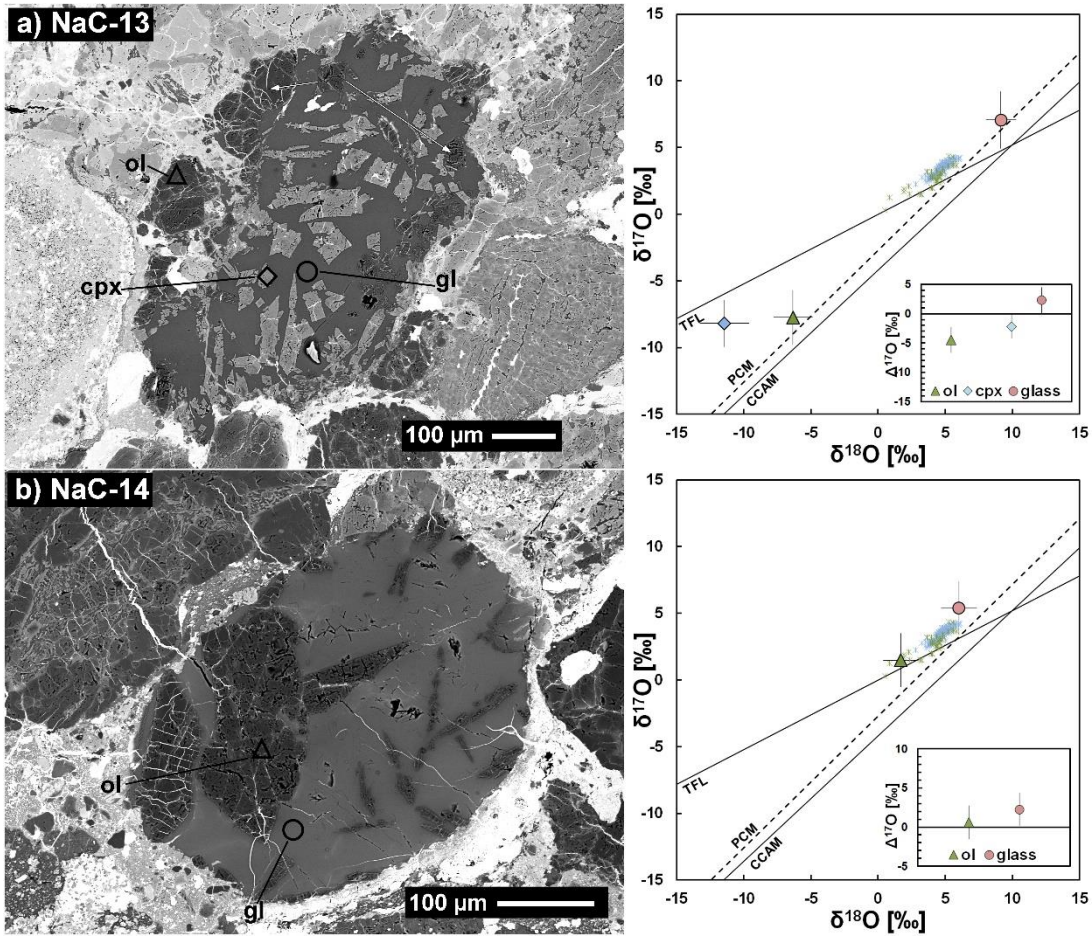
a) NaC-13
ol
cpx
gl
100 µm
b) NaC-14
ol
gl
100 µm
δ17O [‰]
δ18O [‰]
TFL
PCM
CCAM
Δ17O [‰]
ol
cpx
glass

Figure 5:

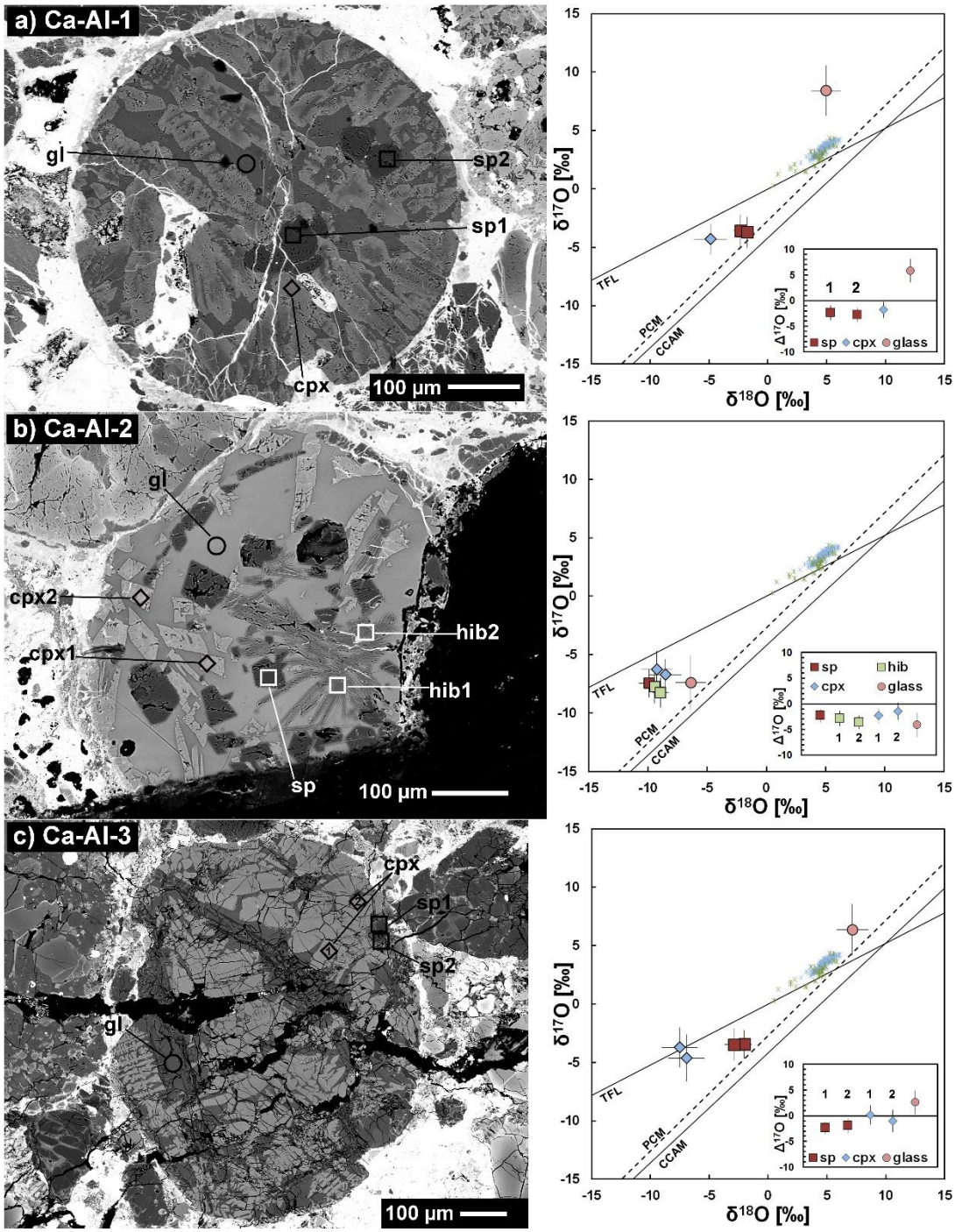
a) Ca-Al-1
gl
sp2
sp1
cpx
100 µm
b) Ca-Al-2
gl
cpx2
cpx1
hib2
hib1
sp
100 µm
c) Ca-Al-3
cpx
sp1
sp2
gl
100 µm
δ17O [‰]
δ18O [‰]
TFL
PCM
CCAM
Δ17O [‰]
sp
cpx
glass
hib
1
2

Figure 6:

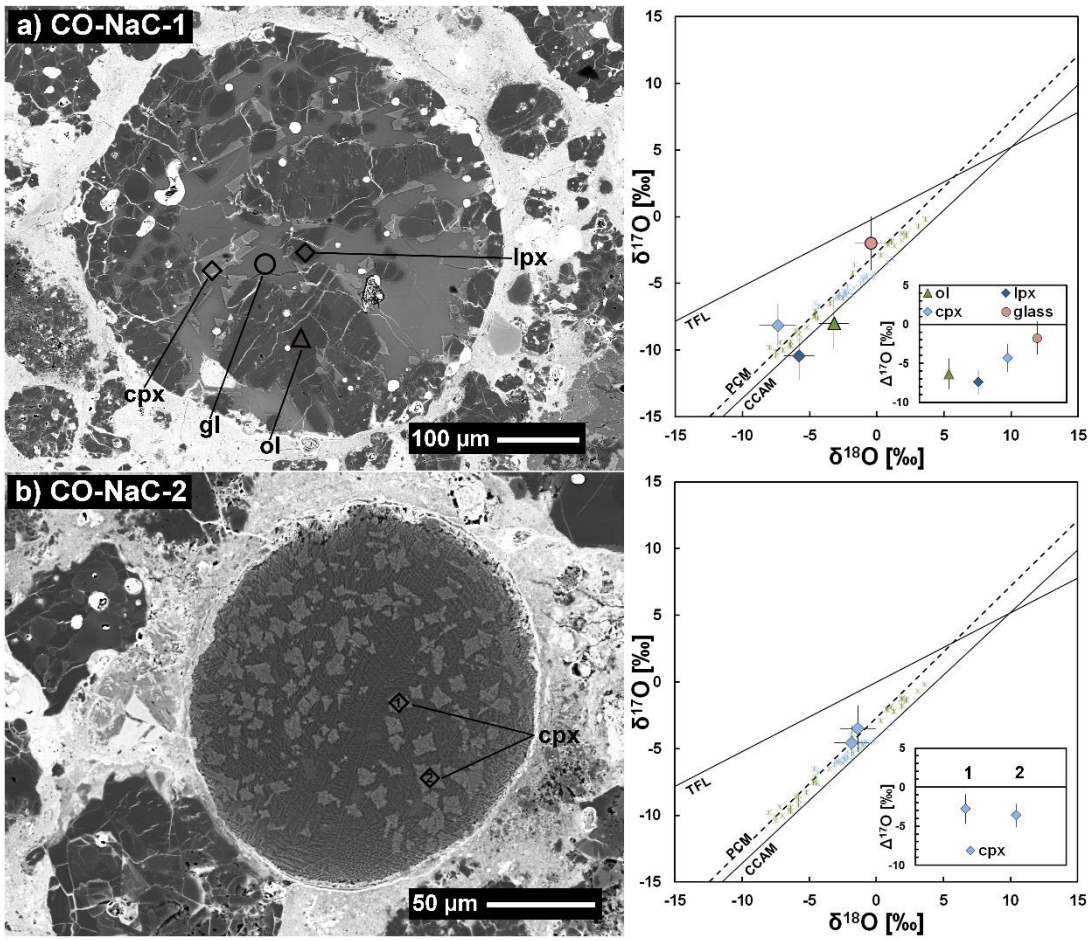
a) CO-NaC-1
lpx
cpx
gl
ol
100 µm
b) CO-NaC-2
cpx
50 µm
δ17O [‰]
δ18O [‰]
TFL
PCM
CCAM
Δ17O [‰]
ol
lpx
cpx
glass
1
2
cpx

Figure 7:

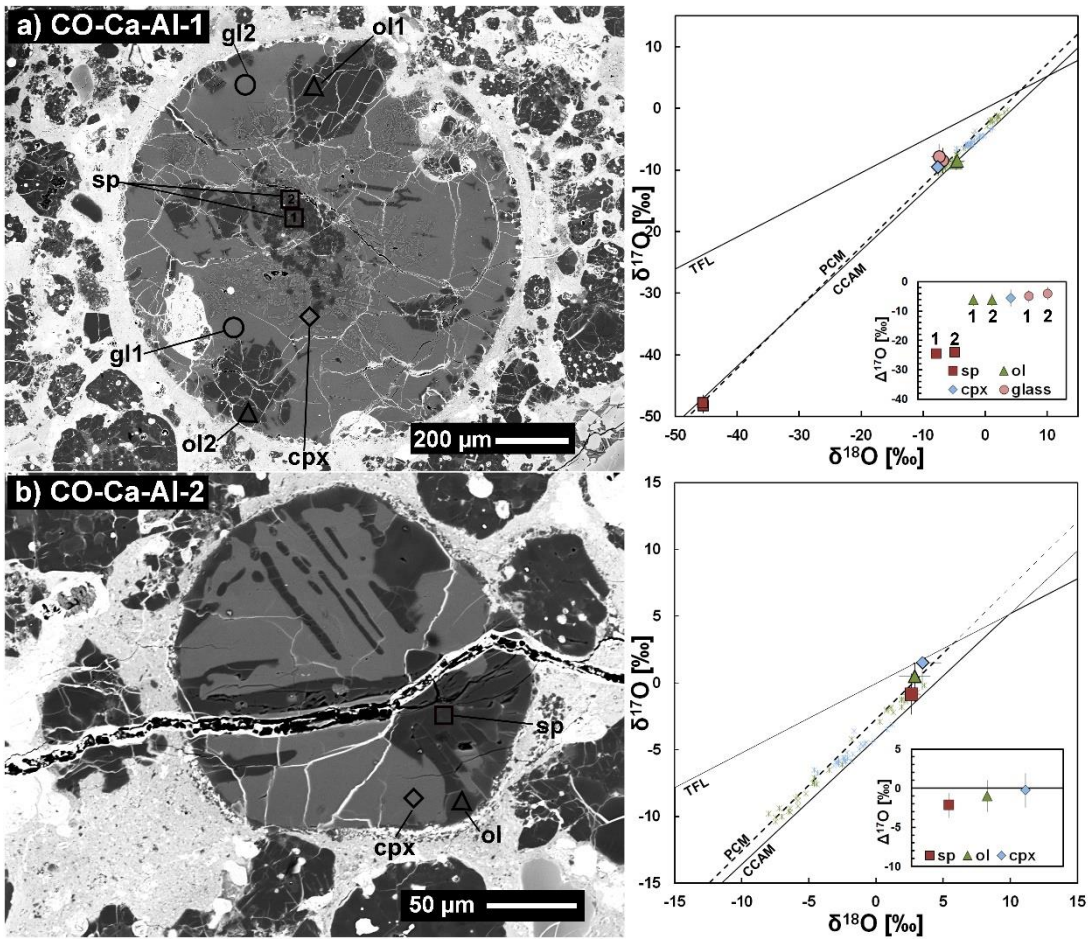
a) CO-Ca-Al-1
gl2
ol1
sp
gl1
ol2
cpx
200 µm
b) CO-Ca-Al-2
sp
cpx
ol
50 µm
TFL
PCM
CCAM
δ17O [‰]
δ18O [‰]
Δ17O [‰]
sp
ol
cpx
glass

Figure 8:

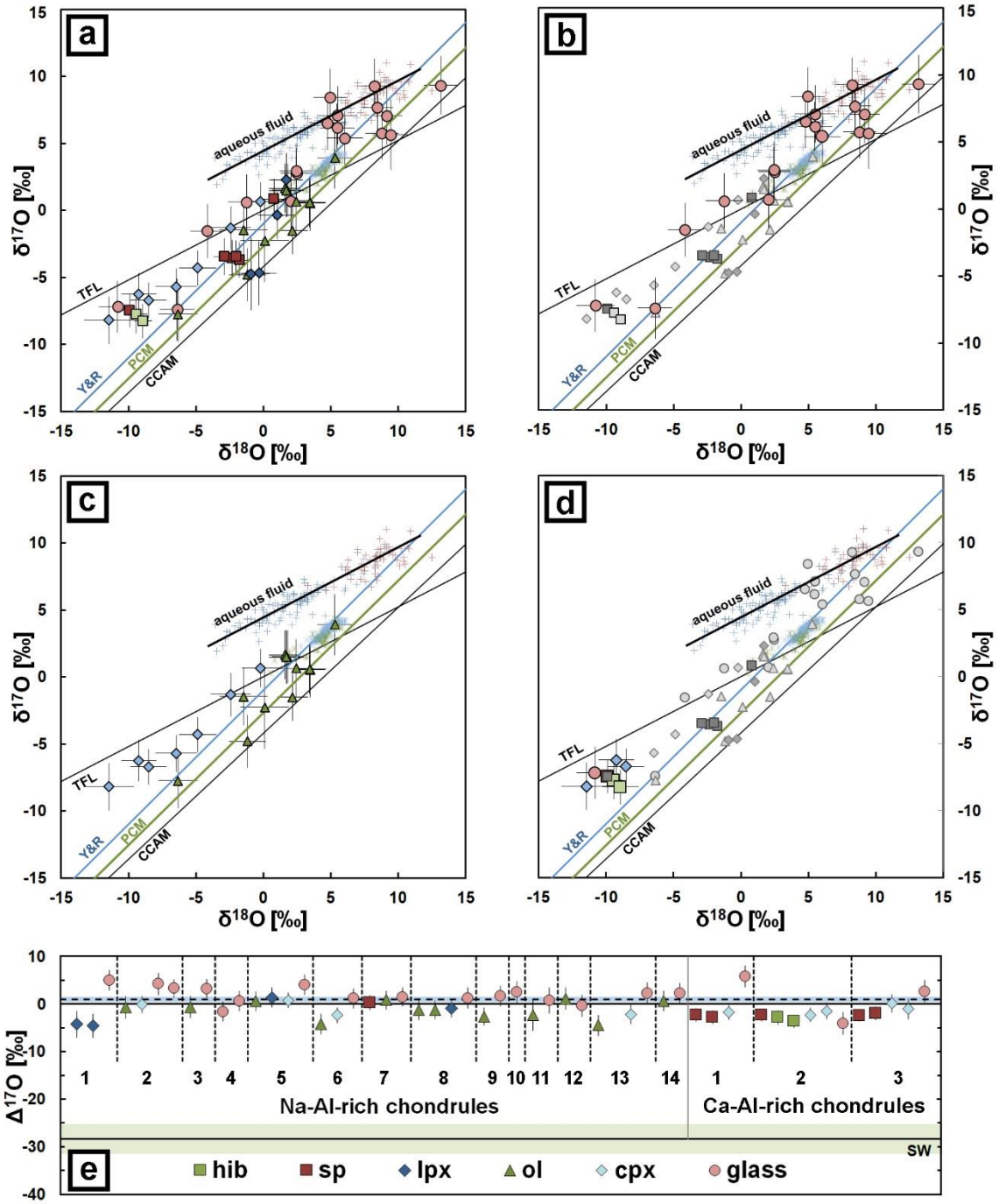
a
b
c
d
e
aqueous fluid
TFL
Y&R
PCM
CCAM
δ17O [‰]
δ18O [‰]
Δ17O [‰]
Na-Al-rich chondrules
Ca-Al-rich chondrules
SW
hib
sp
lpx
ol
cpx
glass

Figure 9:

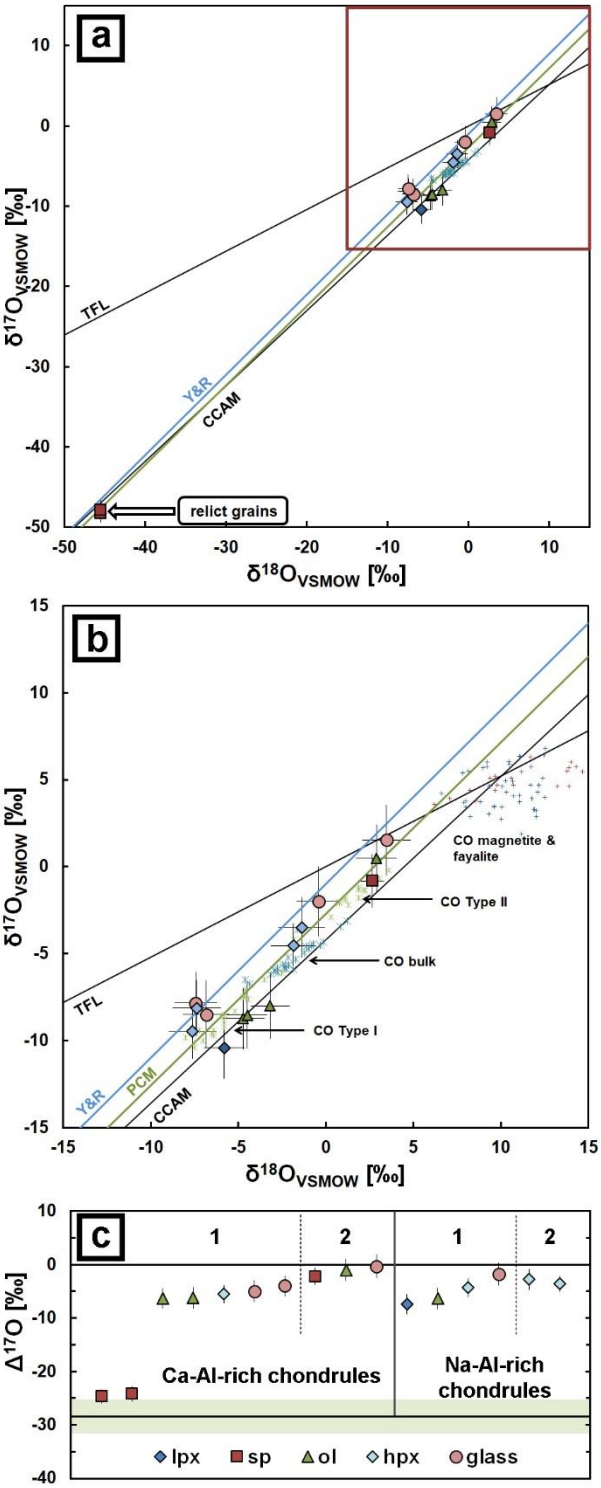
a
TFL
Y&R
CCAM
relict grains
δ17OVSMOW [‰]
δ18OVSMOW [‰]
b
CO magnetite & fayalite
CO Type II
CO bulk
CO Type I
TFL
Y&R
PCM
CCAM
δ17OVSMOW [‰]
δ18OVSMOW [‰]
c
1
2
1
2
Ca-Al-rich chondrules
Na-Al-rich chondrules
Δ17O [‰]
lpx
sp
ol
hpx
glass

Figure 10:

1200

1201

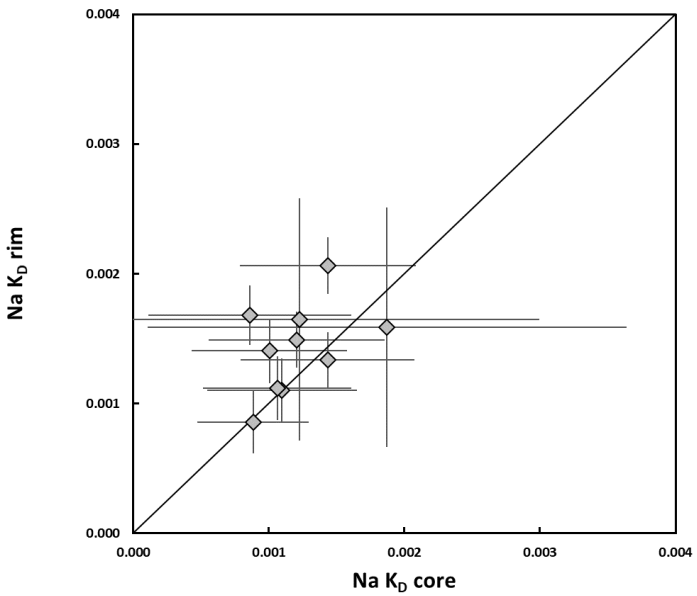
0.004
0.003
0.002
0.001
0.000
Na K_D rim
0.000
0.001
0.002
0.003
0.004
Na K_D core

Figure 11:

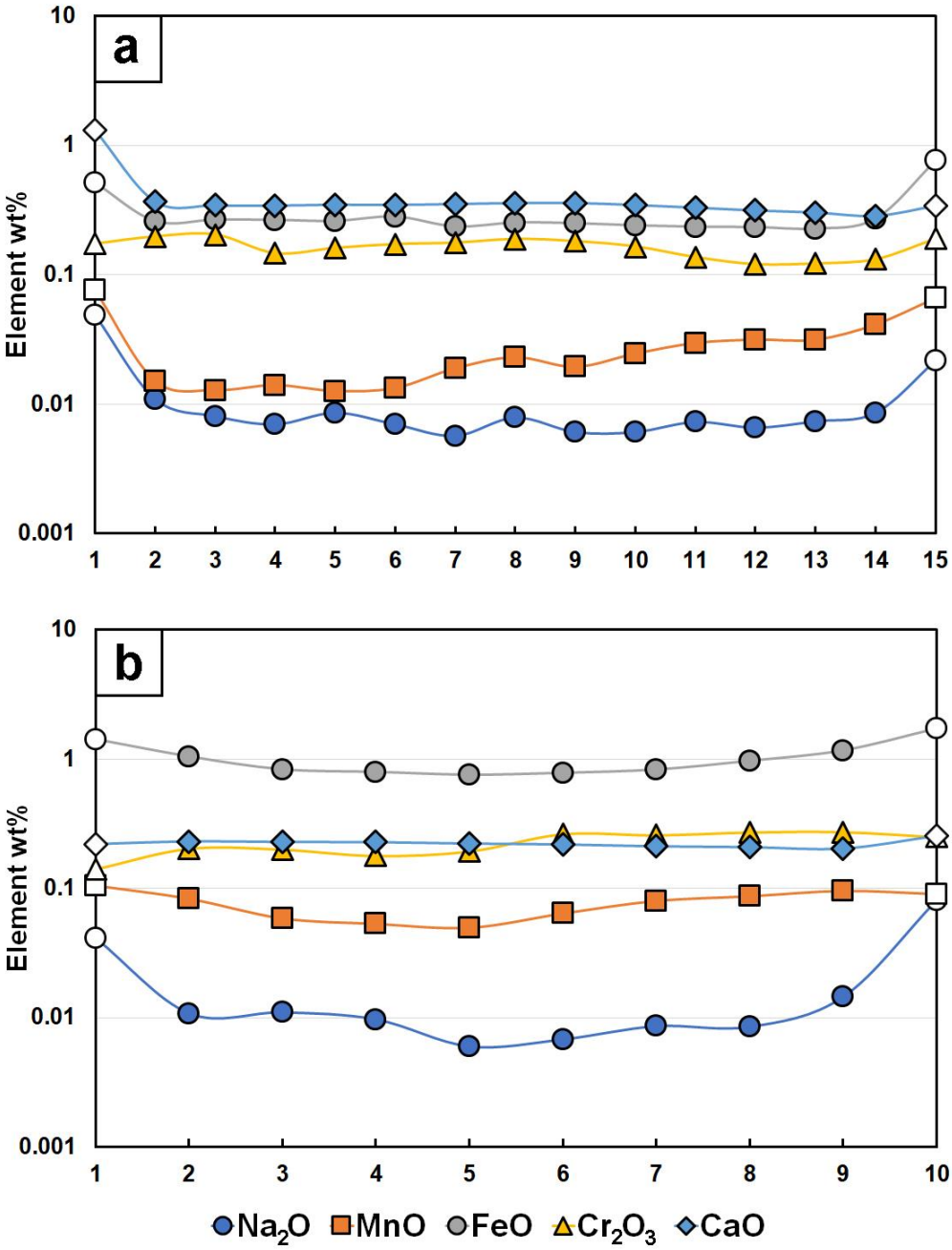
a
b
Element wt%
10
1
0.1
0.01
0.001
1 2 3 4 5 6 7 8 9 10 11 12 13 14 15
1 2 3 4 5 6 7 8 9 10
Na2O MnO FeO Cr2O3 CaO

Figure 12:

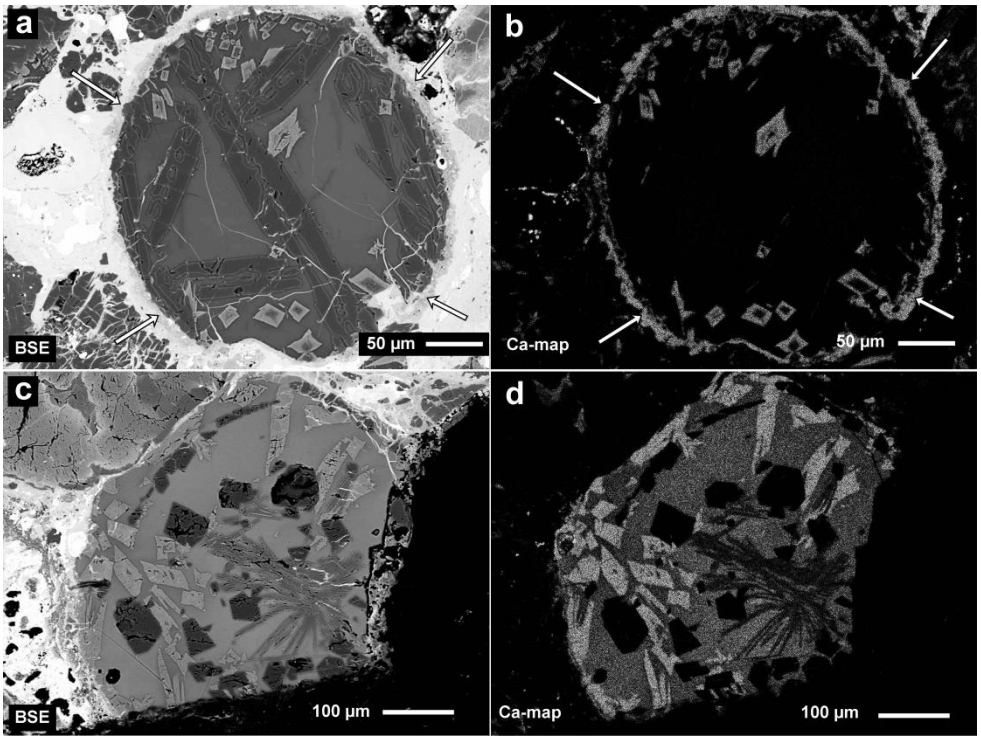

Figure 13: